

The Outflow of the B335 Protostar II: After the Outburst

KLAUS W. HODAPP,¹ ADWIN BOOGERT,² DOUG JOHNSTONE,^{3,4} VALENTIN J. M. LE GOUELLEC,^{5,6} ELENI TSIAKALIARI,⁷ HELEN J. FRASER,⁷ LAURIE L. CHU,⁸ THOMAS GREENE,⁹ AND MARCIA J. RIEKE¹⁰

¹ University of Hawaii, Institute for Astronomy, 640 N. Aohoku Place, Hilo, HI 96720, USA

² University of Hawaii, Institute for Astronomy, 2680 Woodlawn Drive, Honolulu, HI 96822, USA

³ NRC Herzberg Astronomy and Astrophysics, 5071 West Saanich Road, Victoria, BC, V9E 2E7, Canada

⁴ Department of Physics and Astronomy, University of Victoria, Victoria, BC, V8P 5C2, Canada

⁵ Institut de Ciències de l'Espai (ICE-CSIC), Campus UAB, Carrer de Can Magrans S/N, E-08193 Cerdanyola del Vallès, Spain

⁶ Institut d'Estudis Espacials de Catalunya (IEEC), c/ Gran Capità, 2-4, 08034 Barcelona, Spain

⁷ School of Physical Sciences, Walton hall, The Open University, Milton Keynes, MK7 6AA, UK

⁸ National Optical-Infrared Astronomy Research Laboratory, 950 N Cherry Ave, Tucson, AZ 85719

⁹ Caltech/IPAC, 1200 East California Boulevard, Pasadena, CA 91125, USA

¹⁰ Steward Observatory, University of Arizona, Tucson, AZ 85721, USA

Submitted to ApJ

ABSTRACT

The B335 protostar has undergone a major outburst detected in the scattered light of its outflow cavity that has not yet ended. B335 therefore offers the rare opportunity to study its effect on the jet of a protostellar object. Photometry of background stars behind B335 is used to map visual continuum extinction and H₂O ice absorption and demonstrates that the outflow has carved out a cavity. Precise proper motions of the shock fronts emerging from the B335 protostar were obtained. The kinematic age of the most prominent shock front (3E) corresponds to the early phases of the ongoing outburst of the B335 protostar. Shock 3E shows strong CO gas emission, as well as H₂ and [Fe II] emission. Older shock fronts show diminished CO emission and are dominated by H₂ and [Fe II]. The emission feature 0E, closest to the protostar, is distinct in proper motion and radial velocity from the other shock fronts in the jet. In the span of 4'' closest to the protostar, the continuum extinction in front of the outflow cavity increases by $A_V \approx 200$ mag. The CO-line-removed spectra close to the protostar show the unsaturated absorption features of ¹³CO₂, OCN⁻, and OCS have strongly increasing column densities toward the protostar. The ice characteristics are overall similar to those found in lines of sight with less extinction. The central regions of the bipolar nebula show CO gas emission, but at distances of a few arcsec from the protostar, absorption by CO gas is also detected.

Keywords: Star formation (1569) — Bok globules (171) — Young stellar objects (1834) — Protostars (1302) — FU Orionis stars (553) — Stellar jets (1607) — Herbig-Haro objects (722) — Ice spectroscopy (2250)

1. INTRODUCTION

The accumulation of mass from a molecular core onto a protostar proceeds initially by infall of mass from the molecular core onto a circumstellar disk, from which mass is then finally accreted onto the protostar. The accretion process requires a shedding of excess angular momentum via a disk wind and a faster jet, which carve out an outflow cavity into the surrounding cloud and form a bipolar outflow. This outflow is generally detected both at radio wavelengths, most readily in the CO rotation lines, and at near-infrared wavelengths through shock-excited H₂ emission.

The mass accretion onto the protostar is, in general, not a steady process, but is characterized by fluctuations in the accretion rate, and consequently the accretion luminosity, observable as photometric variability of the FUor, EXor or similar types. A list of all known such outbursts has recently been published by Contreras Peña et al. (2025) and the impact of these outbursts on the formation of the star was discussed. As a byproduct of the variations in accretion, the jet velocity is modulated, so that the jets emerging from protostars usually appear as a string of individual internal shock fronts.

The globule Barnard 335 (B335 in short), discovered by Barnard et al. (1927) on wide-field photographs, is part of a larger system of similar globules, but is itself isolated from those other clouds. The protostar in B335 was discovered by Keene et al. (1983) as a far-infrared source. Its isolation and the presence of only one protostar in the globule has made B335 a frequently studied example of isolated star formation. A summary of “Star Formation in Bok Globules and Small Clouds” and B335 specifically was published by Reipurth (2008). B335 has, in the past decade, undergone a major accretion outburst that has not yet completely ended at the time of writing this paper. It offers the rare opportunity to study the effects of an accretion outburst on the outflow and jet emerging from a protostar. Fortunately, B335 was also included in several JWST observing programs of small samples of star-forming regions, so that a uniquely comprehensive data set is available to study the effects of the accretion outburst on the outflow, down to timescales of a few years.

The molecular cloud surrounding the Bok globule B335 was discovered in CO emission by (Frerking & Langer 1982) and mapped in detail by Frerking et al. (1987). The molecular outflow associated with the embedded protostar was discovered by Goldsmith et al. (1984) and then mapped in more detail by Hirano et al. (1988) who also determined that the axis of the large-scale outflow on scales of arcminutes is inclined only by 10° from the plane of the sky, i.e., the bipolar outflow is seen nearly, but not precisely, edge-on.

The bipolar outflow emerging from the single protostar in B335 was further studied by Stutz et al. (2008) based on Spitzer Space Telescope imaging data. Out to a wavelength of $8 \mu\text{m}$ B335 appears as a bipolar nebula. Only at wavelengths of $24 \mu\text{m}$ and longer does it appear as an unresolved point source, probably direct light from the central embedded protostar.

The protostar in B335 is a low-luminosity object, with Green et al. (2013) deriving a luminosity, based on Herschel data, of only 0.68 L_\odot , with an effective T_{bol} of 39K, overall being classified as SED Class 0. Based on more elaborate models, Evans et al. (2023) derives a quiescent luminosity of 3 L_\odot with a peak outburst luminosity of 23 L_\odot . The B335 protostar is a low mass object, with Federman et al. (2026) listing it as 0.25 M_\odot as an approximate consensus value from a large number of individual measurements. Age estimates, discussed in Evans et al. (2023), are in the range of 3 to 4×10^4 yrs.

Numerous outflow shock fronts are found within the outflow cavity. High proper motion shock fronts are found mostly along a fairly narrow jet near the center of the outflow cavity, while low proper motion shock fronts are less concentrated and may be formed by interaction of the outflow with the cavity walls. Optical Herbig-Haro shock fronts emerging from the B335 globule were found first by Vrba et al. (1986) and then confirmed and added to by Reipurth et al. (1992) who labeled them as HH 119 A-C. In the infrared, the first major imaging study was done by Hodapp (1998) who labeled additional shock fronts found in the $\text{H}_2 1-0 S(1)$ emission line, but not confirmed by optical spectroscopy as HH 119 IR 1-5. This naming scheme was expanded to include newly identified shocks by Gâlfalk & Olofsson (2007), who measured the proper motion of the distant shocks detectable at near-infrared wavelengths.

Using purely photometric methods, Olofsson & Olofsson (2009) measured a distance to B335 in the range of 90 - 120 pc. They had already mentioned a possible association of the B335 cloud with the star HD 184982 on the basis that this star appears to be illuminating the cloud in addition to the general interstellar radiation field. Watson (2020) obtained new images of this reflection nebulosity and used the Gaia DR2 distance to HD 184982 of 164.5 pc as a proxy for the distance of the B335 molecular core. Most recent papers on B335 use the rounded value of 165 pc as the distance and we will follow this practice in this paper.

Hodapp et al. (2024) have published a first paper, hereby referred to as Paper I, on the JWST observations of the B335 outflow based on one epoch of observations obtained in 2023. They identified additional highly obscured shock fronts and named them HH119 JWST 0E through 8E for the eastern outflow lobe, and correspondingly for the western lobe. These shock fronts are usually abbreviated to just, for example, 3E, when the context is clear. The naming scheme used in Paper I implies that the shocks appear to occur in east-west pairs, suggesting that they were ejected at the same time. This second paper is based on two epochs, in 2023 and 2024, of JWST/NIRCam imaging in the F444W filter, and one epoch of JWST/NIRSpec IFU observations of the central region of this outflow, done in 2022

(program 1802, P.I.: T. Megeath). Initial results from that NIRSpec IFU program were published by [Rubinstein et al. \(2024\)](#) and [Federman et al. \(2024\)](#).

This paper is structured as follows: The observing methods are outlined in Section 2. The Discussion in Section 3 starts with the overall structure of the B335 cloud core from scattered light (coreshine) in 3.1, and extinction and photometric H₂O ice column density in 3.2. Section 3.3 discusses the photometric variability and local shadow effects in the B335 reflection nebula. Section 3.4 discusses the likely repetitive nature of the accretion outbursts. Section 3.5 presents the results on the B335 outflow and section 3.6 discusses the excitation conditions in the individual shock fronts of the jet. The outflow cavity, outside of the jet, is discussed in section 3.7.

The Appendix A presents results on the proper motion of the B335 protostar from public ALMA observations that are used to identify the position of the protostar at the epochs of the JWST observations presented here. Appendix B outlines the photometric measurement method used to produce the H₂O ice column density map. Appendix C presents results of a component analysis of the ice features in the B335 reflection nebula.

2. OBSERVATIONS AND ANALYSIS METHODS

2.1. JWST NIRCam Observations

The results reported here are based on guaranteed time (GTO) observations with the James Webb Space Telescope (JWST) ([Gardner et al. 2023](#)). The imaging observations are essentially a by-product of the JWST/NIRCam ([Rieke et al. 2023](#)) Wide Field Slitless Spectroscopy (WFSS) of background stars behind B335 aimed at mapping the column density of H₂O, CO₂, and CO ice (program 1187). Details of our sample selection and preliminary ground-based results on the onset of ice formation in the selected cores (B68, L694-2, and B335) was presented by [Chu & Hodapp \(2021\)](#). The extinction mapping of the B335 molecular core will be published in a separate paper.

While this program on B335 was originally planned to be done in a single epoch, a guide star acquisition error during visit 15:1 in 2023 necessitated, or better, allowed, a repeat observation of the failed visit one year later. Fortunately, both the 2023 and 2024 visits covered the region around the B335 protostar in the F444W filter, the only filter to show the heavily obscured inner, and youngest, shock fronts of the B335 outflow. The resulting two-epoch F444W dataset is therefore ideally suited for proper motion measurements of the inner, youngest shock fronts, whose proper motion has not been measured previously. However, the more distant shock fronts to the east of B335, HH 119 IR 3, 4, and 5 in the terminology of [Hodapp \(1998\)](#) were not covered in the second epoch and no new proper motion data were obtained. The imaging observations presented here were carried out on 2023 April 25 UTC (MJD 60059.080) and on 2024 April 24 UTC (MJD 60424.258), quite precisely one year apart. We have obtained images in the F070W, F090W, F115W, F150W, F200W as parallel observations with the short channel of NIRCam, and images in F277W, F300M, F356W, and F444W as the main observing program with the long channel of NIRCam. [\[DATASET\]](#)MAST

Results from the 2023 imaging WFSS observations with some proper motion information based on older ground-based observations were presented in the first paper in this series on B335 by [Hodapp et al. \(2024\)](#), hereafter Paper I.

2.1.1. Astrometry

The reduced images from MAST are nominally astrometrically calibrated, but that calibration was found to be of insufficient quality for a comparison of shock proper motions, probably because of the scarcity of Gaia catalog stars in and near the dark cloud. The NIRCam F444W images at the two epochs were not taken at exactly the same position on the sky. As a first step in aligning these two images, approximately matching cutouts containing the central region of the outflow were produced. We used two methods for aligning these two cutout images. A set of reference stars visible on both epoch F444W images was selected, excluding saturated, very faint, and overlapping stars. There are no foreground stars toward the B335 globule, so this sample represents stars at a distance greater than that of B335. Due to the absorption in the B335 cloud, none of these stars are optically visible and therefore, none of them have Gaia positions or proper motions. It is reasonable to assume that such a large ensemble of stars at various, but unknown, distances is a close approximation of the celestial reference system, but systematic effects of streaming motions in the background star field can not be excluded. For the second method, we used a sample of small extended sources not looking like shock-excited outflow features. The expectation is that this is a sample of somewhat compact extragalactic sources that have negligible proper motions. For the purpose of fine-aligning the two images, we magnified them by a zoom factor of 30. We measured the correlation of both images on both sets of objects, varying rotation and spatial offsets in integer steps in the zoomed image. The background star sample contains more objects, and for each, the

position can be correlated with better precision. While determining the correlation of the extragalactic sources is less precise than for stars, the sample is expected to be a more accurate representation of the reference frame. Both background object samples gave closely similar results and in the end, we used the mean of the two measurements of the spatial offsets to match the two images. The correction in row and column direction 26 ± 2 and 22 ± 2 mas, respectively, i.e., less than half of one pixel in the original data. The field rotation was found to be zero. This procedure results in the two images having matching sky coordinates, even though the absolute accuracy of these coordinates has not improved by matching the background objects in the two epoch images. The problem remains that the whole B335 cloud, and, in particular, the protostar embedded in it, cannot be expected to be stationary in front of the background stars.

We have measured the proper motion of the protostar itself, which is not detected at near-infrared NIRCam wavelengths, on public ALMA data. The procedure is detailed out in Appendix A.

The position of the B335 protostar is:

$$\alpha(t) = 294.25369864 + 2.62 \times 10^{-6} \times (t - 2000.0),$$

$$\delta(t) = 7.56940726 - 5.33 \times 10^{-6} \times (t - 2000.0) \text{ with } t \text{ in years.}$$

This measured proper motion of the B335 protostar in the one-year epoch difference of 8 mas in RA and -18 mas in DEC was applied as a final step in the alignment process to the matched F444W images, so that, instead of being referenced to the mean background star positions and extragalactic reference positions, the final two images are instead registered with respect to the position of the protostar.

As explained in detail in the Appendix A, the measured projected velocity of the B335 protostar is 16.7 km s^{-1} at a position angle of 154° . It is an order of magnitude smaller than the proper motions of shock fronts in the jet emanating from the protostar. We only use these relatively aligned images for the purpose of shock front proper motion measurements. For the purpose of displaying the absolute coordinate system in the various figures in this paper, we rely on the world coordinate system (WCS) produced by the STScI pipeline. The comparison of the two epoch of imaging data indicates that this WCS is accurate to better than one half of a NIRCam pixel. The WCS of the NIRSpec IFU data cube is less precise, as was noted, for example, in [Wang et al. \(2025\)](#). Fortunately, there is one background star detected in the NIRSpec IFU data that is also detected in the NIRCam F444W image. Assuming that the NIRCam data are more accurate, and the star has negligible proper motion in the ≈ 9 months between the NIRSpec and the 2023 NIRCam images, we have used this star to measure the NIRSpec IFU offset relative to NIRCam of $0''.24$, and applied this correction. The resulting corrected protostar position in the NIRSpec data cube, calculated for the epoch of the NIRSpec IFU observations, is astrophysically plausible and is shown in all figures based on the NIRSpec data.

2.1.2. Shock Proper Motion Measurements

The individual shock fronts were labeled in Paper 1 (their Figure 1), and are again identified here in Section 3.4, Figure 6. The emission knot closest to the protostar, 0E, does show some motion between the 2023 and 2024 images. It shows CO, but little shock-excited H₂ and [Fe II] emission. On the western side of the outflow, knot 0Wn did not move measurably between 2023 and 2024, but it does show CO, H₂ and [Fe II] line emission. The shock front identified as 1E in the 2023 data (Paper 1) changed its appearance so much in 2024 that we could not measure a proper motion with confidence. The proper motions of most individual knots of shock-excited emission were measured by computing the correlation of the 2023 and 2024 images in selected sections containing only the knot in question, while varying the spatial offset between the two image sections. The maximum of the correlation matrix gives the shift of the knot between the two images, i.e., the proper motion. For the complex bow shocks at larger distance from the protostar, we have tried to divide the shock front up into smaller sub-regions. For the faint shock fronts 2E, and the knots immediately next to the protostar, 0E, 0Wn, and 0Ws, we had to resort to measuring the proper motion by tracking the flux maximum of the knots on contour maps. The knots in this region close to the protostar were not sufficiently separated spatially for the cross-correlation technique to work reliably. The errors of the proper motion measurements are dominated by the complexity of the flux distribution and the changes in the shape of the shock-excited knots over the course of the year between the observations. We estimate that in the best case the isolated, small and bright shock front 3E can be measured with one pixel error in the zoomed image, i.e., approximately 2 mas. On the other hand, the faint shock 2E, situated in complex extended reflection nebulosity, can probably only be measured to a precision of 20 mas. The variability of the reflection nebula and the measured proper motion vectors will be discussed in sections 3.4 and 3.5.

2.1.3. *Faint Extended Emission: Cloudshine*

The coreshine effect in B335 was studied on the basis of a set images with uniform pixel scale of 0.030 arcsec pixel⁻¹ in all the filters used by us for B335 imaging: F070W, F090W, F115W, F150W, F200W, F277W, F300M, F356W, and F444W. The shortest wavelengths show the B335 cloud as a featureless area of absorption against the background, while at the longest wavelengths, scattered radiation from the protostar at the outflow cavity dominates. Figure 1 shows a false-color representation of three of the shorter wavelength (F090W, F150W, and F277W) images where scattering reveals useful information about the cloud structure. The cross sections through our images shown in Figure 2 were extracted in broad stripes of 400 pixel width in RA, and 4200 pixels length in DEC. All pixels above a certain small threshold were excluded from the computation of the sky level to eliminate images of stars and the diffraction spikes of bright stars located outside of the stripes. Fainter extended features from the reflection nebula and shock-excited regions are retained in the stripes so processed. In each row (400 pixel extent), we sorted all remaining pixels, and computed the median of the 5th to 16th faintest pixel in this sorted set. Essentially, this is close to a noise-clipped minimum signal. This process further suppresses the signal from stars and star diffraction spikes, but also eliminates low signal noise spikes.

2.2. Photometry of Background Stars

Generating the maps of extinction and H_2O ice column density starts with a flux-limited list of stars in the field observed with NIRCam in B335. This star list was carefully visually inspected and detector defects, artifacts from diffraction spikes, extragalactic extended objects, and closely spaced stars were excluded. In a second iteration of this process, stars directly behind knotty, shock features were excluded. For all stars in this curated list, aperture photometry was performed in the F277W, F300M, F356W, and F444W filters. Since the signal in the F300M filter, designed to match the H_2O ice absorption band, was the faintest of these filters, all stars with F300M photometry fainter than 1 μJy had their photometry marked as invalid.

Each star with valid photometry in all those four filters represents a column density (or extinction) measurement in a line of sight through the molecular cloud. This set of randomly distributed line-of-sight measurements can only be processed into a contiguous map with some assumptions. We have chosen a technique minimizing assumptions about the structure of the molecular cloud. For each position on the sky within the images, the assigned water ice column density is the weighted median column density in the closest seven lines of sight (stars) with valid photometry. We found that the weighted median combining of several lines of sight is essential for eliminating noise spikes produced by low S/N individual stars. The resulting column density map is therefore an irregular patchwork of small areas of constant column density. It is an unfortunate side effect that those patches of constant column density are largest in areas of high column density, i.e., close to the protostar, where detectable background stars are scarce.

2.2.1. Continuum Extinction

The color of each star is a combination of its intrinsic color, the interstellar extinction in the background and unrelated to B335, and the extinction in B335 itself, the latter being the quantity of interest. While the intrinsic color of each background star could, in principle, be determined from spectroscopy, this is not a realistic option for most of these faint background stars. We rely instead on the fact that the intrinsic colors of stars in the infrared vary much less than the expected effects of many magnitudes of A_V . This same assumption was made by [Lada et al. \(1994\)](#) in their seminal paper on infrared extinction measurements. We can measure the average color of the background star field near B335, but not significantly affected by absorption in this cloud, in module B of NIRCam, which pointed to an essentially unobscured background star field during our imaging of B335 in module A. We measured the average color or H_2O ice index, respectively, in this reference field and subtracted this average from the B335 field shown in Figures 3 and 4.

Our restriction to using only two wavelengths, i.e., one color as an estimate of extinction was necessitated by the fact that the other available long wavelength filters (F300M and F356W) are substantially affected by the H_2O ice absorption, and in the short wavelength filters, the extinction is so high that no stars are detectable in the area of interest near the protostar and the outflow cavity. The continuum color based on the synthetic “F277W-F300M” (Appendix B) and the F444W AB magnitudes was used to create the continuum extinction map discussed later in section 3.2. F444W is strongly affected by CO_2 and CO ice absorption, but these are fairly narrow features. The filter is not affected by H_2O ice absorption.

By only using long-wavelength data points, this map is sensitive to the high extinction values near the core of B335. Similar to the map of H_2O ice column density, this map also shows the reduced line-of-sight extinction in the outflow cavities. We used the near-infrared extinction law by [Wang & Chen \(2019\)](#), their equation 10, with a power-law index of -2.07 to convert the measured color excess to usual unit of A_V . Our continuum extinction map has better spatial resolution, but a much smaller area coverage than the extinction map by [Chu & Hodapp \(2021\)](#), which was based on ground-based J, H, and K photometry with UKIRT and Spitzer channel 1 and 2 data. That larger area map also shows the reduced extinction in the outflow cavities at larger distances from the protostar and in regions of overall much lower extinction values. The resulting patchy extinction map is certainly not the true structure of the molecular cloud, but it is the closest approximation that our data directly support. We display this map in greyscale in the lower panel of Figure 3 for A_V . For the contours overlayed in Figure 3, we have smoothed this map with a Gaussian of sigma = 15 pixels.

2.2.2. H_2O Ice Column Density from Photometry

The optical depth of the broad absorption feature of H_2O ice can be approximately measured using filter photometry of background stars behind the B335 molecular core. We used photometry in the F277W, F300M, F356W, and F444W filters. Our method of calculating an approximate H_2O ice optical depth and column density from this filter set is

explained in the Appendix B. In this paper, we will use this photometric H_2O ice column density map only for qualitative and morphological arguments. A more detailed study of the ice features in the B335 cloud on the basis of more NIRCam WFSS spectra will be published in a separate paper in the future. We used the band strength of $A = 2.0 \times 10^{-16} \text{ cm molecule}^{-1}$ for amorphous water ice at $T = 25\text{K}$ recommended by [Bouilloud et al. \(2015\)](#) as the presently best consensus value. The resulting map of the H_2O ice distribution is thus calibrated in units of molecules cm^{-2} . We display this photometric H_2O ice column density map in greyscale in the lower panel of Figure 4. For the contours overlayed in Figure 4, we have smoothed this map with a Gaussian of sigma = 15 pixels.

2.3. NIRSPEC IFU

We use the publicly available NIRSpec IFU spectroscopy obtained under GO program 1802 (P.I. T. Megeath) to extract spectra of selected knots, and to try to determine proper motions. [\[DATASET\]](#)MAST The data on B335 were obtained on MJD 59838.0 (2022 Sept. 16). Spectral images based on this data set have already been published by [Federman et al. \(2024\)](#) and extracted spectra in the east and west outflow lobe have been presented and discussed by [Rubinstein et al. \(2024\)](#). For our analysis, we used the data cube produced by the STScI pipeline. We extract the flux in specifically selected smaller regions of the outflow lobes so that individual shock fronts and changes in the scattered continuum light can be studied.

3. DISCUSSION

3.1. Overall Structure of the B335 Core from Scattered Light, Coreshine

At optical and near-infrared wavelengths, B335 appears as a small dark cloud slightly elongated in the north-south direction, or, as we will discuss in the following, better described as flattened in the east-west direction. A “shadow” minimum in the extended flux seen by [Stutz et al. \(2008\)](#) at $3.6\mu\text{m}$ and $8.0\mu\text{m}$ to the south of the protostar, and also pointed out in our Paper I, is clearly associated with the nearly complete absence of background stars in this area of the cloud. This finding at longer infrared wavelengths confirms the flattened shape of the B335 core at higher column densities.

Infrared polarimetry of background stars was used by [Hodapp \(1987\)](#) to map the magnetic field structure in B335. A similar study over a larger field by [Kandori et al. \(2020\)](#) obtained very similar results in the core, but also measured the field star polarization in the off-core, low-extinction field, which showed similar degrees of polarization than the on-core field. Subtracting the off-core polarization, caused by the anisotropic general interstellar extinction, revealed a cleaner “hourglass” pattern of the in-core polarization vectors. From these two studies, and the even wider field result by [Bertrang et al. \(2014\)](#), it is clear that the magnetic field traced by near-infrared polarization is parallel to the axis of the outflow, and that the core of the molecular cloud is flattened in that same direction, nearly east-west. Much closer to the protostar, ALMA dust emission polarization measurements by [Maury et al. \(2018\)](#) and [Le Gouellec et al. \(2023\)](#) confirm that the outflow axis is aligned with the magnetic field and find that the magnetic field in the disk around the protostar is in north-south direction, i.e., perpendicular to the outflow axis.

The B335 globule is larger than the field of view of a single module of NIRCam, in particular at short wavelengths where the lower extinction regions show cloudshine. We therefore used a reference position farther away from B335 in NIRCam Module B as the blank sky reference region. This region was carefully selected to be free of bright stars and diffraction spikes from bright stars. Using effectively the minimum of the signal measured in this region as the sky value, we subtract this from the crosscuts shown in Figure 2. The crosscuts in the F150W (blue) and F200W (green) filters begin and end with signal above zero, indicating the field of the NIRCam Module A was not sufficient to cover the full spatial extent of the cloudshine interstellar scattered light. At the longer wavelengths covered by the NIRCam long-wave channel, i.e., in filters F277W (yellow) and F356W (red), the crosscut signal starts and ends near zero. At the short wavelengths, shown blue and green, the crosscuts show a minimum of cloudshine flux near the position of the protostar (left panel), in other words, the scattered light is concentrated in a rim around the cloud center. This minimum in the scattered light gets narrower with increasing wavelength. In the F277W filter (yellow), light scattered off the walls of the outflow cavity, i.e., the reflection nebula, produces a maximum of flux in the crosscuts.

The image in Figure 1 also shows that the scattered light in the F090W (blue) and F150W (green) filters shows a minimum in the area of the eastern (blue-shifted) outflow cavity. There are a number of bright stars in that area, but these have Gaia distances of ≈ 540 pc or farther, and are distant background objects behind B335. There is no indication of any light scattering from these stars off the B335 cloud at optical wavelengths, e.g., in the deep images by [Gâlfalk & Olofsson \(2007\)](#), so there is no reason to reopen the question of distance to B335.

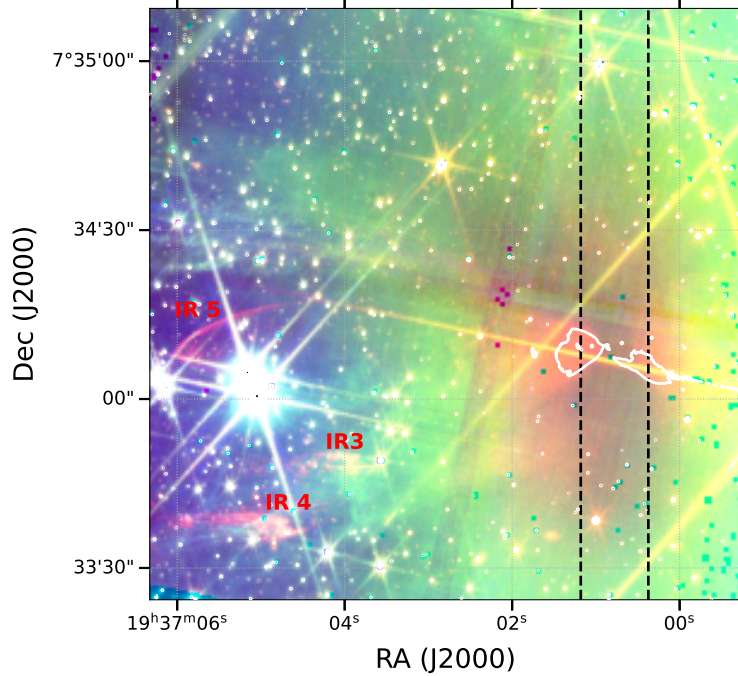


Figure 1. RGB color composite sky-subtracted image of the B335 outflow: F277W, F150W, F090W. This image clearly shows the “core shine” scattered light from the interstellar radiation field outlining the B335 cloud and core. The densest parts of the core, where the protostar is located, are seen as a depression in the scattered interstellar light, showing in a brownish color. In the center of this dark region, in the F277W filter images displayed in red, the bipolar reflection nebula, illuminated by the protostar appears in reddish color. A few contours (white lines) of the flux in the F444W filter are included to show the knots in the inner jet and the outline of the inner outflow cavity. The distant parts of the outflow cavity appear as a region of reduced scattered light in the eastern part of the image. The B335 cloud only contains one flattened dense molecular core. The extent of the stripe used for extracting the crosscuts shown in Figure 2 is indicated by dashed lines. We have added labels (in red) for the distant shock fronts (appearing pink in this RGB image) in the eastern lobe, since this figure is the only one in this paper showing these shock fronts.

In comparison to the extinction and column density maps presented in the next subsection, the cloudshine and coreshine data extend to regions of lower density in the perimeter of the molecular core and demonstrate that the outflow cavity can be traced into those peripheral regions of the molecular core.

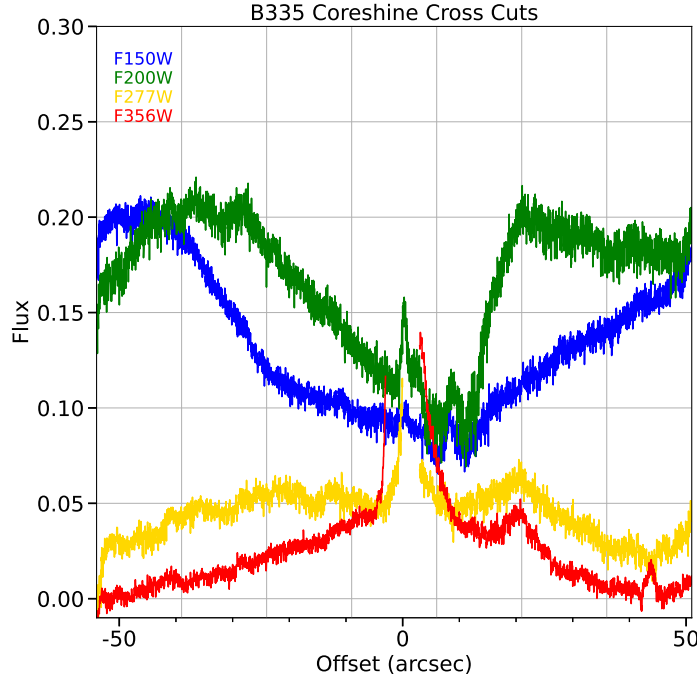


Figure 2. Crosscuts in declination direction centered on the protostellar source (offset 0), between the dashed lines in Figure 1. The crosscuts are colored in wavelength order and the filters used are indicated. At the shortest wavelength (F150W, blue), B335 appears as a dark cloud against the background, the apparent size of which gets smaller with increasing wavelength (F200W, green). At even longer wavelengths, the reflection nebula illuminated by the protostar begins to be detectable (F277W, yellow), and becomes dominant in the F356W filter (red)

3.2. H_2O Ice Column Density and Continuum Extinction Maps

Figures 3 and 4 show maps of the H_2O ice column density in units of cm^{-2} and the continuum extinction in units of A_V . The lowest contour on the A_V map is $A_V=5$ mag, roughly corresponding to the edge of the dark cloud at optical wavelengths. The B335 core appears as a roughly ellipsoid shape, with the long axis approximately in the NS direction and, more to the point, the short axis lying in the EW direction. In B335, the magnetic field is roughly oriented in EW direction near the position of the protostar (Kandori et al. 2020). This suggests that the core was initially formed by contraction along the field lines of the local magnetic field, as was first theoretically predicted by Mestel & Spitzer (1956) and further developed by Shu et al. (1987). The result of this contraction is the flattened overall structure of the B335 core, seen apparently nearly edge-on and therefore appearing elongated in the north-south direction in the extinction maps.

The outflow activity originating at the single protostar has carved out bipolar outflow cavities. Both in the continuum and in the H_2O ice column density map, lines of sight through the outflow cavities show lower extinction than other areas of the core, leading to an hourglass shape of the contours. The same hollowed-out outflow cavity seen in Figure 1 in scattered light was also already indicated in the near-infrared extinction map by Chu & Hodapp (2021). The hollowed-out outflow cavity was first formed by a wind from the protostar, pushing material out from its surrounding molecular core. The outflow cavity at present contains a very hot jet and is limited by a layer emitting in shock-excited H_2 , so overall, it is too warm to allow the formation of dust and ice mantles, and therefore appears as a region of lower extinction and ice column density.

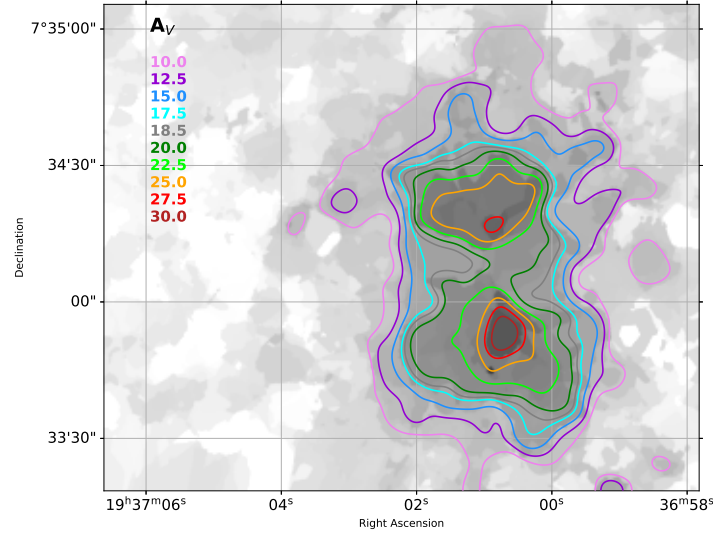
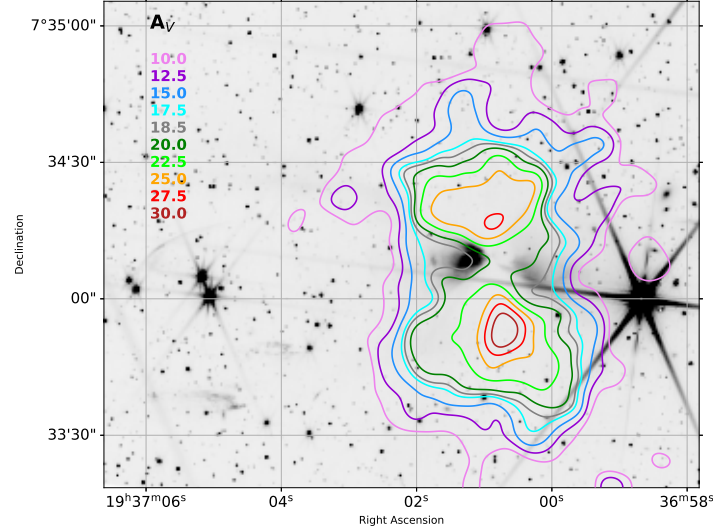


Figure 3. Top: Cutout of the F356W image with smoothed ($\sigma = 15$ pixels) contours of the continuum extinction overlaid, to demonstrate the relation between the outflow cavity and the cloud structure. The outflow cavity is traced by the bipolar reflection nebula. Bottom: The continuum extinction map in its original resolution shown in greyscale with smoothed contours of that map overlaid.

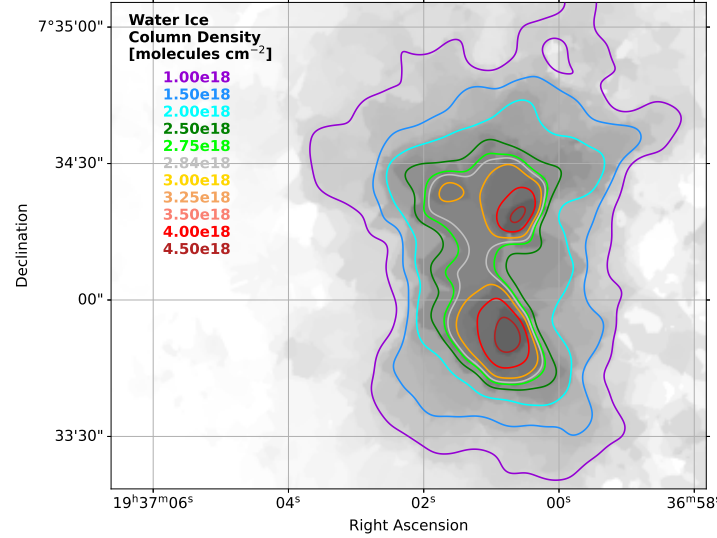
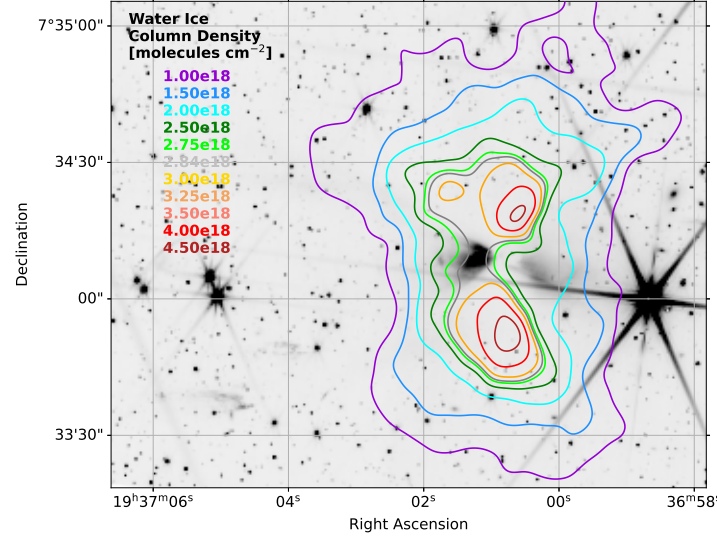


Figure 4. top: Cutout of the image in F356W with smoothed ($\sigma = 15$ pixels) contours of the H₂O ice column density overlaid. The outflow cavity is traced by the bipolar reflection nebula. Bottom: The H₂O ice column density map in its original resolution shown in greyscale with smoothed contours of that map overlaid.

We note that the extinction map underestimates the column density in the region immediately south of the protostar, where even in the F444W filter, no stars were detected. The mapping algorithm therefore fills this region with the median column density of stars detected in the less obscured perimeter of this opaque region, and therefore underestimates the column density in the opaque region itself. Considering this opaque region, the protostar is not located in the densest part of the B335 core. The simplest explanation may be that much of the material in the protostar's immediate surroundings may already have fallen onto the disk, and a large fraction of it may already have gone through the accretion disk and been ejected again as a disk wind or as the jet, in the process sculpting the region around the protostar and blowing material out of the outflow cavity. Of course, some fraction of this material will have properly been accreted onto the protostar. The hollowed-out structure of the cavity follows closely the walls of this cavity seen in ALMA molecular line emission, as is shown, for example, in Figure 1 of [Le Gouellec et al. \(2023\)](#).

3.3. Variability of the Reflection Nebula

Bipolar nebulae associated with protostars are commonly understood to be primarily reflection nebulae with an additional component of line emission, mostly shock-excited H₂. Infrared polarization observations for Class I and II objects typically show the large degrees of polarization and an orientation perpendicular to the outflow axis expected from scattering, as first pointed out by Hodapp (1984), and shown in spatially resolved detail for many bipolar nebulae. Such polarimetric observations have not been done specifically for B335, due to its extreme extinction, but there is no doubt that B335 contains reflection nebulosity.

The variability of the B335 reflection nebula was found and discussed in detail by Evans et al. (2023), on the basis of data from the WISE/NEOWISE space telescope (Wright et al. 2010). At the wavelength of the WISE W1 and W2 filters, only the reflection nebula is detected and variability of the protostar is indirectly inferred.

At millimeter radio wavelengths, based on ALMA CO data in various isotopologues, Cabedo et al. (2021) and Bjerkeli et al. (2023) observed infalling gas towards B335 and concluded that a disk is being formed. Bjerkeli et al. (2023) noted that the infall kinematics suggest episodic infall.

It should also be noted that variability of B335 was also noted earlier at radio wavelengths by Avila et al. (2001). The CO outflow of B335 and its changes after the present outburst were discussed by Kim et al. (2024). The fact that the B335 nebula can show strong variations on timescales of a few years shows that it is largely a reflection nebula. At its distance of 165 pc, the light travel time is 0.95 days for one arcsecond in the plane of the sky. Changes in the illumination from the protostar during an accretion outburst therefore propagate across the nebula in approximately one month, while, on the other hand, physical movement of material, even in the fast jet, takes of order of a century, as we list in Table I. Variability due to changes in the shock excitation would therefore be expected to be on such a longer timescale.

We add to this discussion in Figure 5 by putting our two epochs of NIRCam imaging into the context of the on-going decline of the lightcurve of B335. Both the light curves in the WISE W1 and W2 bands show that, compared to the original WISE data points between MJD 55000 and 56000, the light curve has not returned to that level. In particular, the shorter wavelength W1 light curve (in magnitudes) appears to have stabilized about halfway between the maximum and the earliest recorded W1 photometry. The two earliest epochs of WISE data, in the cryogenic operations phase, already indicate an increasing brightness, both in W1 and W2. We therefore have to assume that those early WISE measurements do not represent a true quiescent condition of the protostar, but rather some early stage in the on-going outburst, or that a truly quiescent state does not exist in B335 so that low-level variability is always present. The measured outburst amplitude is at least 3.5 mag in W1, and the outburst duration exceeds 5000 days, indicating a duration and amplitude similar to the few classical FUor outbursts for which the infrared outburst amplitudes have been compiled by Contreras Peña et al. (2025). B335 is a member of the still very small subgroup of very deeply embedded protostars exhibiting long-duration outbursts of similar amplitude and duration as some classical FU Orionis stars. The first example of such an object was OO Ser (Hodapp et al. 1996), with a similar overall appearance to B335 (Hodapp et al. 2012). A more recent example is HOPS 383 discussed by Safron et al. (2015).

Figure 6 shows the ratio of the 2023 and 2024 F444W images, so that local changes on top of the overall variability are visible. There are a number of straight features in the ratio image pointing back at the position of the protostar (coordinate origin in Figure 6), most noticeably at the northern edge of the blueshifted (eastern) lobe of the bipolar nebula. These straight features cannot be explained by shock fronts or thermal effects. We interpret these features in our ratio images as shadows cast into the reflection nebula by local variations in the illumination and absorption from the immediate surroundings of the protostar. They indicate that the light path illuminating the reflection nebula contains absorbing dust condensations moving substantially on a timescale of one year. We also have to assume that these absorbing dust condensations are above the plane of the disk around the protostar, so that shadow effects can be produced in the reflection nebula. A simple estimate on the basis of Keplerian motion around an object of 0.25 M_⊕ gives an orbital period of 2.0 years at 1 AU distance. While we cannot determine what orbital motion of a dust condensation is producing the changes observed within our one-year epoch difference, a distance from the protostar in the range of a few AUs appears as a reasonable estimate. We note again that the light travel time for the extent of the reflection nebula is of order one month, short compared to this estimate of orbital period, so that the formation of straight shadows is expected.

Similar straight features in the temporal ratio or difference images have been noted before in other variable reflection nebulae. Hubble's Variable Nebula NGC 2261 (Hubble 1916), illuminated by the variable young star R Mon is arguably the best studied case and shows both the slow moving straight shadow effects pivoting around the position of the illuminating star (Lightfoot 1989) as well as the faster moving light echos (Lightfoot & Scholz 2025). In the more

deeply embedded L483, an object similar to B335 in that it is also a very young low mass protostar in an isolated small globule, [Connelley et al. \(2009\)](#) found evidence for straight shadow effects. The phenomenon of straight shadows in variable reflection nebulae has also been observed in much larger and higher luminosity deeply embedded objects like Cep A by [Hodapp & Bressert \(2009\)](#) and also, based on optical images, in a less obscured YSO: the EXor variable V1647 Ori studied by [Aspin et al. \(2009\)](#).

In typical protostellar outflow objects, see, for example, the review by [Ray & Ferreira \(2021\)](#), and specifically in B335, a fast jet is propagating along the central axis of the outflow cavity, which is carved out of the surrounding molecular core by a slower disk wind. Following the model proposed by [Lightfoot \(1989\)](#), our finding of shadows implies that somewhere between the jet and the outflow cavity wall, density enhancements (clumps) in the rotating disk wind are launched onto spiraling paths, and partly obscure the scattering optical path, leading to the observed shadow effects. The amplitude of the shadow fingers is of order 20% in the F444W filter, i.e., the optical depth changes in the scattering light path are less than unity wavelengths around $4.4\ \mu\text{m}$.

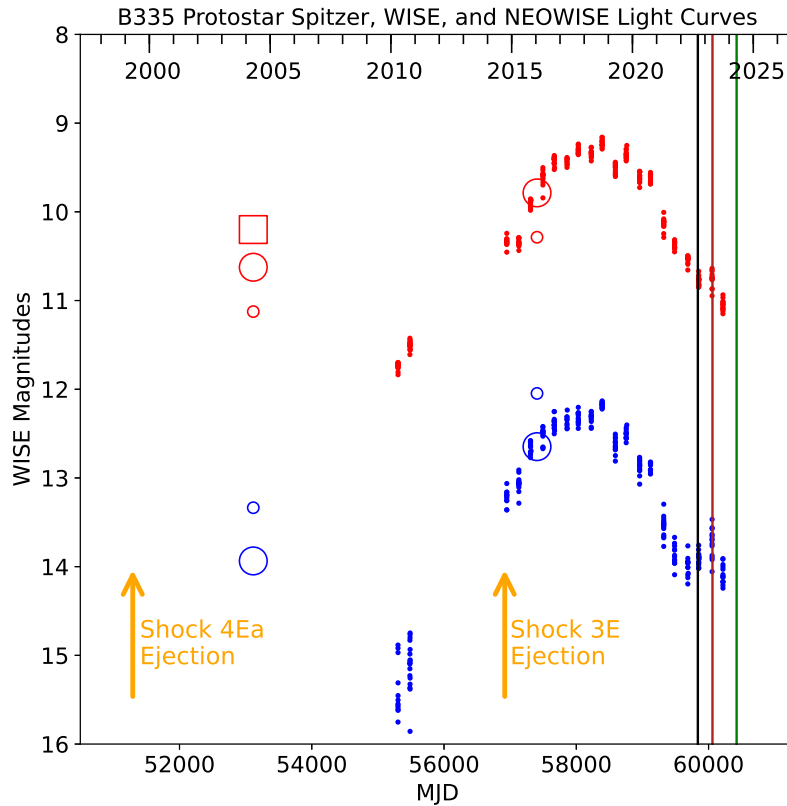


Figure 5. NEOWISE W1 and W2 light curve in Vega magnitudes. The epoch of the NIRSpec IFU (MJD 59838.0, 2022 Sept. 16, black line) and the two epochs of NIRCam imaging 2023 04 25 UTC (MJD 60059.1, 2023 Apr. 25, brown line, and MJD 60424.3, 2024 Apr. 24, green line) are indicated by vertical lines. We have also included the photometry based on Spitzer images in 2004 and 2016. The open red square is the large-aperture magnitude from [Kim et al. \(2024\)](#), the open circles are our raw and corrected $r=4''$ magnitudes. We have indicated the ejection times of shocks 4Ea and 3E. Shock 3E was ejected in the early phase of the presently on-going outburst. The wind causing shock 4Ea was plausibly ejected during the earlier outburst indicated by the 2004 Spitzer photometry.

In Figure 7, we show a cross-cut of the ratio of the 2024 image to the 2023 image through the reflection nebula along the line indicated in blue in Figure 6. At large distance from the outflow cavity, the ratio is near unity, even though

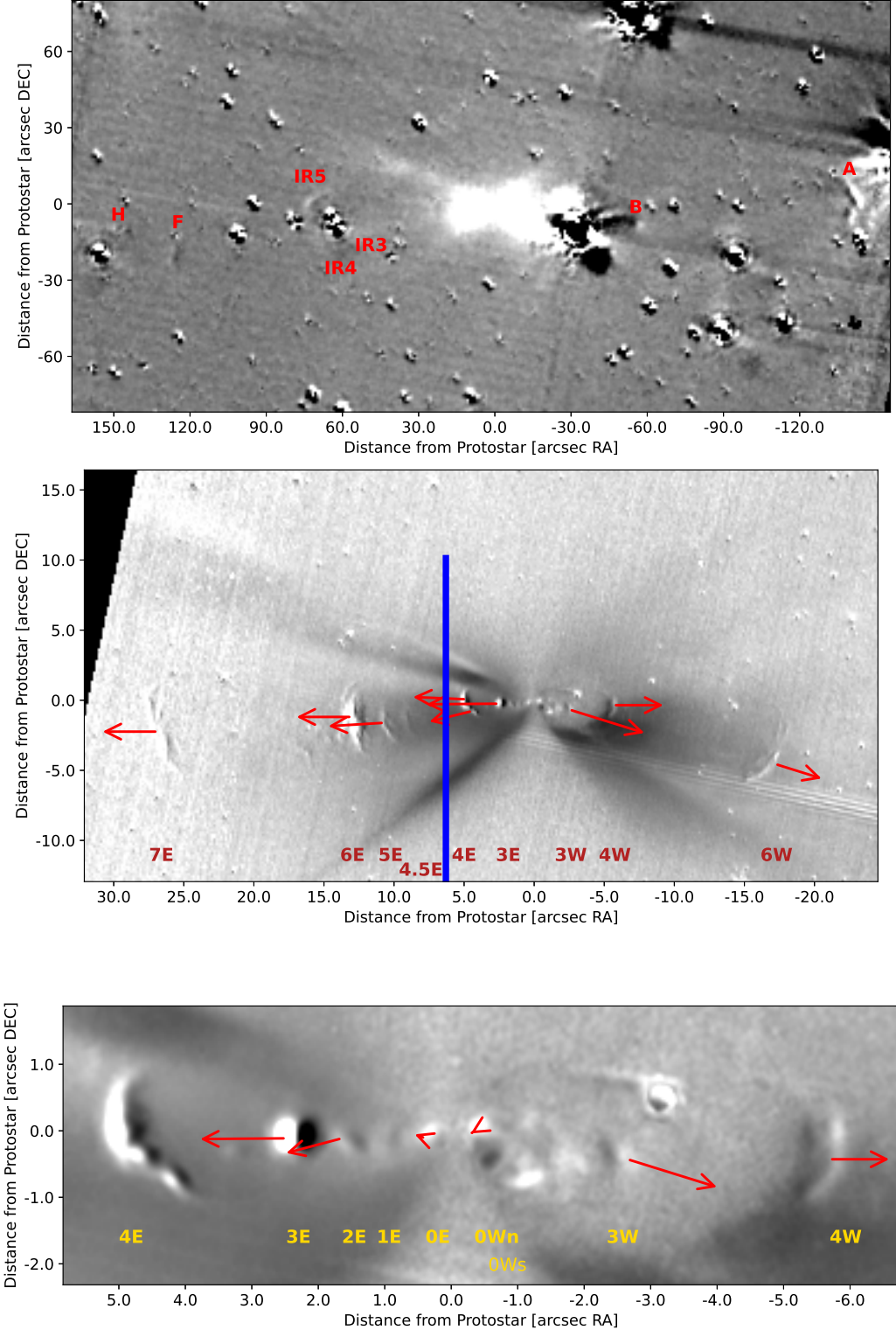


Figure 6. Top Panel: Wide field difference image of Spitzer channel 2 images of B335 taken in 2004 and 2016. The coordinates are offset from the position of the protostar. Moving shock fronts are seen adjacent pairs of black (2004) and white (2016) images of the same object. The previously known shock fronts are labeled. Shock fronts IR3 and IR4 do not show noticeable shifts in the images. We conclude that these are nearly stationary shocks, and not part of the fast jet. Middle Panel: Shock proper motion vectors overlaid on the ratio of the registered NIRCam F444W images at the two epochs: April 25, 2023 and April 24, 2024. The grayscale was chosen so that local changes in the illumination pattern in the reflection nebula are apparent. The middle panel is the overall view of the B335 reflection nebula and shock front, the lower panel is zoomed in on the innermost shock fronts. The images at the two epochs are registered to a common position for the protostar. Due to the proper motion of the protostar, all background objects appear to have slightly moved in the year between the two epochs. The proper motion values are listed in Table I.

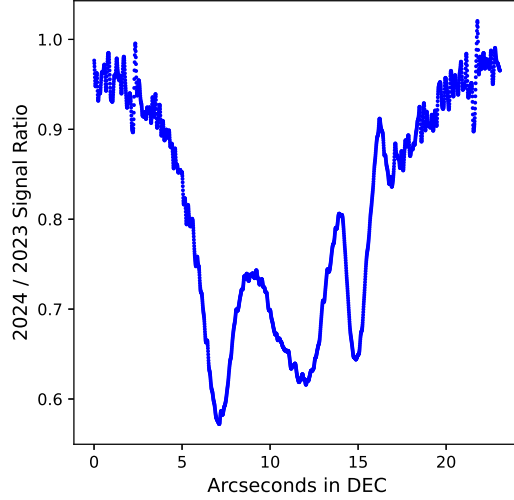


Figure 7. Crosscut from south to north through the B335 outflow cavity along the line indicated in blue in Figure 6. Shown is the flux ratio of the 2024 and 2023 F444W images. On average, the flux in 2024 was only ≈ 0.7 of the 2023 flux, but substantial local variations of order 20% are seen, indicating strong shadowing variations on timescales of one year, i.e., an order of magnitude shorter than the timescale of the overall brightness outburst of B335 documented in Figure 5.

noisy due to the faintness of the extended emission. In the outflow cavity, the ratio drops, on average, to ≈ 0.7 , but with local variations of ± 0.1 .

3.4. Are there Repetitive Outbursts ?

The chain of shock fronts emerging from the B335 protostar certainly suggests repeated ejection events. There is only one set of Spitzer channel 1 and 2 images available that were obtained prior to the WISE/NEOWISE missions, on MJD 53116, referred to here simply as 2004. [Kim et al. \(2024\)](#) have extracted photometry from the channel 2 image in a large 12'' aperture and have corrected for the difference in the bandpass between Spitzer and WISE. Their channel 2 photometric point at 10.2 mag is indicated in Figure 5 by an open square. It indicates that the protostar was brighter in 2004 than in the earliest WISE observations.

We have analyzed the same archival Spitzer image with a different strategy. We used a smaller, $r=4''$ aperture centered on the blue-shifted outflow lobe. We have also used a set of Spitzer channel 1 and 2 images obtained on MJD 57406 (2016) for the study of background star extinction in B335 by [Chu & Hodapp \(2021\)](#). The difference of the Spitzer 2004 and 2016 images has already been shown by [Hodapp et al. \(2024\)](#) to illustrate the local variations in the brightness variations.

We show the uncorrected extracted photometry as small open circles in Figure 5 and have used the 2016 photometry to determine the offset to nearly contemporaneous NEOWISE measurements. This offset, accounting for the different integrating apertures used, was then applied to the 2004 data, the result being shown as large open circles in the lightcurve.

While our data point lies 0.4 mag fainter than the larger aperture photometry by [Kim et al. \(2024\)](#) our data, in both Spitzer channel 1 and 2, confirm that in 2004, B335 was in a state of brightness comparable to the average, not the maximal, brightness of the present (2018 maximum) outburst. This is a tentative indication for an outburst prior to the present one and makes it likely that shock front 4E, with ejection dates of individual components around 1999 (Table 1), was ejected during this prior outburst.

3.5. The Outflow

Our imaging in Paper I and the spectral images discussed by [Federman et al. \(2024\)](#) show several distinct components of the bipolar nebula associated with the B335 protostar. A wide reflection nebula seen primarily at continuum wavelengths is probably limited by the cone angle of the continuum radiation emanating from the immediate surroundings of the protostar. The variability of these components, and the fact that the variability is not uniform but shows structure indicating shadow effects originating from near the protostar, all point in the direction of the nebula being defined by the limited solid angle of illumination emanating from the protostar and the disk surrounding it. The column density maps demonstrate that there is plenty of dust outside of the reflection nebula that could potentially scatter light, but that this dust is simply not being illuminated from the protostar. It is also clear from the comparison of line images by [Federman et al. \(2024\)](#) (their Figure 3) that emission of shock-excited H₂ traces an outflow cone that is narrower than the walls of the outflow cavity reflection nebula.

Based on near-infrared images, [Hodapp \(1998\)](#) discovered and [Gâlfalk & Olofsson \(2007\)](#) measured the proper motion of the large, more distant shock fronts in B335. To avoid confusion between their naming terminology, IR 3, 4, and 5, from the scheme used by [Hodapp et al. \(2024\)](#) (Paper I) and in this paper, they are identified again in Figure 1. For these, we could not obtain a new proper motion measurement because the second epoch image did not cover these shocks.

We show a difference image of two Spitzer Space Telescope channel 2 images, obtained in 2004 and 2016, to give an overview of the larger-scale outflow in Figure 6 (top panel) and to qualitatively confirm the large proper motion of the shock fronts in the jet, in particular A, B, IR5, F, and H). The two Spitzer images, taken with the same instrument 12 years apart, represent a very consistent data set. However, apparent changes in the shape of individual shock fronts make it an oversimplification to just quote a single proper motion value for each shock front. The proper motion away from the protostar is apparent in the differential image. This statement includes the large bow shock 5 in [Gâlfalk & Olofsson \(2007\)](#), “IR5” in [Hodapp et al. \(2024\)](#), for which [Gâlfalk & Olofsson \(2007\)](#) has measured a high proper motion (245 km s^{-1}), similar to the jet shock fronts that we will discuss here. A noteworthy exception are the shocks IR3 and IR4, where we do not see the same differential (black-white) pattern. These complicated shocks do not move with anything close to the speed of the jet in B335. In the Spitzer data, they are consistent with being stationary. [Gâlfalk & Olofsson \(2007\)](#) lists 25 km s^{-1} for IR3 and 16 km s^{-1} for IR4a. We conclude that these are shocks in the much lower velocity disk wind or an entrained lower velocity wind that is carving out the cavity, possibly shocking against the stationary cavity walls.

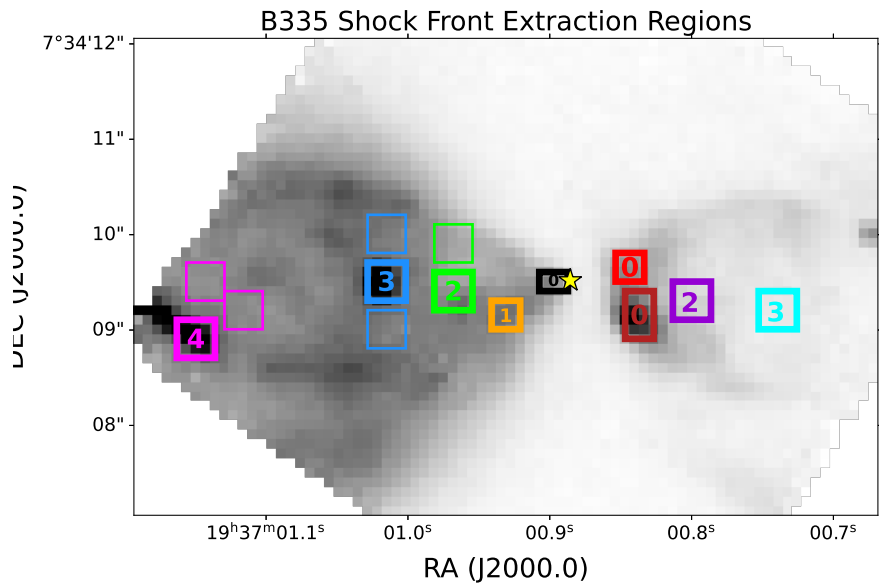


Figure 8. Positions of the regions for NIRSpec IFU datacube spectrum extraction. The color coding corresponds to the colors of the spectra in Figures 9 to 14. The image is the data cube slice at a wavelength of $5.053 \mu\text{m}$, centered on an H_2 emission line. Thick outlines and labels indicate the extraction regions for shock-excited emission features, thin outlines are the reflection-only “cavity background” regions used for scattered light subtraction. The position of the protostar at the epoch of the NIRSpec observations is indicated by a yellow star symbol.

Near the central axis of the outflow, a narrow jet indicated primarily by the high-excitation atomic line of [Fe II] has been identified by [Federman et al. \(2024\)](#), their Figure 3. This central jet was studied in more detail by [Federman](#)

Table 1. B335 Shock Fronts

Identification	RA	Dec	PM mas yr ⁻¹	PM [km s ⁻¹]	PA [deg]	Kin. Age [yr]	Eject Year
HH119 JWST 7E	294.26104	7.56845	206	161	90	130	1983
HH119 JWST 6E	294.25722	7.56895	204	160	99	62	1961
HH119 JWST 5E	294.25660	7.56875	208	163	93	51	1972
HH119 JWST 4Ea	294.25506	7.56929	200	156	88	24	1999
HH119 JWST 4Eb	294.25498	7.56919	210	164	91	22	2001
HH119 JWST 4Ec	294.25486	7.56910	167	131	104	25	1998
HH119 JWST 3E	294.25433	7.56927	266	208	90	8.6	2014
HH119 JWST 2E	294.25413	7.56926	181	141	105	8	2015
HH119 JWST 0E	294.25378	7.56927	42	33	70		
HH119 JWST 0Wn	294.25359	7.56931	12	10	121		
HH119 JWST 3W	294.25306	7.56920	290	227	-107	8	2015
HH119 JWST 4W	294.25225	7.56897	187	146	-90	28	1995
HH119 JWST 6W	294.24930	7.56795	183	143	-107	93	1930

et al. (2026) on the basis mostly of MIRI MRS IFU spectra in [Fe II], [Ni II], [Ne II], and [Ar II]. They find that the blue- and red-shifted jets are at a 168.5° relative to each other, not at 180° as simple symmetry would predict. Their finding is consistent with the appearance of other, more distant shock fronts in our images, e.g. in Figure 6, where shocks 3W and 6W are not axisymmetric to shocks 3E and 6E, and their proper motion vectors are not anti-parallel. For other shocks, most notably 4E and 4W, this misalignment is less pronounced, which could be explained by the finding by Federman et al. (2026) that the B335 jet axis “wiggles”. Some of the jet knots are also prominent in Br α . The strongest shock front in the jet, 3E, is also detected in H₂, but the other jet knots in [Fe II] are not prominent in H₂ emission. Table I, lists the measured proper motions of the shock fronts that we could study in our images.

The bright, compact shock front 3E has proper motion of 208 km s⁻¹ and a radial velocity of -84 km s⁻¹ (Figure 11) relative to the systemic velocity represented by the average of 0E, 0Wn, and 0Ws. For the next shock in the blue-shifted lobe, shock 4E, we can distinguish three components, listed separately in Table I. Only the most southern of these components (4Ec) is included in the field of the NIRSpec data cube. In Figure 11 the CO emission lines in shock 4E (violet lines) appear less blue-shifted than those of shock 3E (blue lines) and correlation with the spectra of 0E, 0Ws, and 0Wn gives a radial velocity of -28.5 ± 2.5 km s⁻¹ for 4Ec, the southern component in shock 4E (Table I), very different from 3E indeed. It should also be noted that the ¹²CO ro-vib lines of shock 3E are quite likely optically thick and suffer from self absorption effects, so that the measured radial velocity is dominated by the surface of the shock facing the observer. In shock 3E, like in all other internal shock fronts in the jet, gas is being squeezed perpendicular to the jet axis, expanding the shock front sideways. This is clearly demonstrated by the morphological changes going from shock fronts 3E to 4E, 5E, 6E out to IR5. The high blueshifted value of the 3E radial velocity probably just represents the surface facing the observer of a laterally expanding shock front.

Therefore, the radial velocity of the bulk of gas in shock 3E is probably lower than the measured value. Our radial velocity measurement allows to set an upper limit for the inclination of the velocity vector against the plane of the sky of 22° of course assuming the distance to be 165 pc. This upper limit is consistent with the 10° inclination determined by Hirano et al. (1988) from the original larger-scale mapping of the outflow in CO emission and a model of the outflow structure. We note that a determination of the inclination angle by Stutz et al. (2008) based on radiative transfer models gave an inclination of only 3° from the plane of the sky. It should also be noted that the motion of any individual shock front cannot be expected to follow the axis of the outflow cavity precisely, since Federman et al. (2026) has found clear evidence that the B335 jet has wiggles, and shows evidence for some precession of the jet axis. Therefore, any determination of the outflow axis on the basis of shock kinematics can only refer to the momentary condition at the time of the ejection of the material that later shocks against other outflow components.

From the proper motion and the distance from the position of the protostar, we have determined the kinematic ages of the shock front prior to the epoch of the first NIRCam images in 2023. For the bright shock front 3E, we have

indicated this kinematic age by an arrow in Figure 5, indicating that its launch coincides with the early phase of the photometric outburst that is, at present, in its declining phase.

From their position-velocity diagrams based on CO emission observations taken in 2017 with ALMA, [Bjerkeli et al. \(2019\)](#) found a high-velocity feature named the “molecular bullet” with a very short kinematic age of only 1.7 yr, i.e., launch in early 2016, again coincident with the early phase of the present phase of increased accretion luminosity. Based on the same data set, [Kim et al. \(2024\)](#) analyzed this high velocity component in more detail and put it in relation to the on-going infrared outburst. The high-velocity blue-shifted (-30 km s^{-1}) in the 2017 ALMA data is almost certainly related to shock front 3E observed by us. Shock 3E, being part of a larger jet of shock fronts, must be an internal shock front in that fast jet, where younger, newly ejected and faster jet components run into, and shock against, older, slower jet gas.

3.6. Changes in Shock Excitation Conditions Along the Jet

In the following, we discuss individual shock fronts, first the shocks in the eastern, blue-shifted lobe, in order of distance from the protostar. Then, secondly, we discuss the knots in the western, red-shifted lobe. The first set of apertures for spectral extraction, shown in Figure 8, are the shock-excited emission knots previously identified in Paper 1. For shocks 2E, 3E, and 4E, we made an effort to subtract flux contributions from the background and foreground cavity emission. The cavity-background boxes are outlined by thin lines in the same color as the shock extraction box. For the other shocks, 0E, and 0Wn and 0Ws, this procedure was not possible because they are so close to the protostar that no suitable background region could be identified.

3.6.1. Shock 0E

The emission knot closest to the position of the protostar in the eastern, blue-shifted outflow lobe is shock 0E (Paper I). In the difference image of the 2023 and 2024 images, a position shift is noticeable in knot 0E and listed in Table 1; however, this proper motion is much smaller than the motion in the other emission knots further downstream in the jet. The spectrum of 0E can be decomposed into a very steep continuum spectrum, and an emission line spectrum dominated by CO line emission. The CO lines of shock 0E have similar radial velocity as 0Wn and 0Ws, the related knots in the other outflow lobe. Together, these three knots closest to the protostar have a very different, lower, radial velocity than shock 3E, the brightest and youngest shock in the central jet. They also have slower proper motion than shock 3E. Shock 0E is clearly not part of the jet ejected from the protostar. The protostar is not directly visible in the NIRCam and NIRSpec wavelength range out to $5.0 \mu\text{m}$. Shock 0E appears faint due to the very high extinction in the protostellar disk seen from the side. The difference images of H_2 and CO emission in shock 0E shown in Figure 15 shows that H_2 emission extends in a broad paraboloid cone east of the protostar position, while CO is concentrated at the apex of this cone and of the [Fe II] jet. This CO emission knot is the closest feature to the protostar position detected in this NIRSpec data set. However, it is not coincident with the position of the protostar from ALMA observations, reduced to the epoch of the NIRSpec data, that is indicated by a star symbol in Figure 15. The extraction box for the 0E spectra in Figure 9 encompasses this CO-dominated region close to the protostar. The spectrum, shown in black, is dominated by the emission of CO gas, with H_2 and [Fe II] lines only roughly as strong as the typical CO line.

The difference image of H_2 and [Fe II] in Figure 15 shows the distinct [Fe II] jet that emerges from the protostar, while H_2 emission is outlining the cavity walls, probably excited by shocks from a much slower disk wind. In the spectral images shown by [Federman et al. \(2024\)](#), the CO emission is concentrated in a cone of roughly the same width as the H_2 emission, but does not extend as far down along the outflow axis. This suggests that the CO emission is produced under similar temperature conditions as the H_2 emission, but is limited to higher density regions.

[Rubinstein et al. \(2024\)](#) published an analysis of the CO excitation conditions based on population diagrams for a larger sample of protostellar objects, including the innermost outflow lobes of B335, one of them being close to our cutout definition of 0E, the other encompassing 0Wn and 0Ws. They identify two temperature components (900K and 1700K) based on the ν 1-0 transition and a higher temperature component of 6300K based on the ν 2-1 transition.

The shocks further downstream (4E, 6E [Hodapp et al. \(2024\)](#)) show a diminishing fraction of CO emission. Also, the spectra of the cavity walls themselves, being illuminated by the same radiation from the protostar, show little CO emission. We have already concluded (Section 3.3) that the continuum seen in 0E is scattered light from the protostar. In contrast, the CO emission in 0E is not scattered radiation emanating from the protostar itself. The proper motion data, and the radial velocity of 0E (but also 0Wn and 0Ws) being different from the fast jet shocks (the strongest being 3E) suggests that the CO emission is produced by a stationary or low velocity shock in a disk wind.

3.6.2. Shocks 1E and 2E

The ratio image Figure 6 shows the typical dark-bright pattern of a moving shock front at the positions of shock 1E and 2E. Knot 1E, identified in paper I, appeared less defined in 2024 and a proper motion could not be measured with confidence. Shock 2E (Figure 9) only shows very weak CO emission, in distinct contrast to the strong emission in shock 3E discussed below, even though it has similar proper motion.

We interpret these two weak shocks as low relative velocity internal shocks in the fast jet material that was launched at the beginning of the photometric outburst. We cannot associate the ejection times of these faint shocks with any specific feature in the light curve.

We want to point out already that on the western side of the bipolar outflow, we see a pattern of faint, rather disorganized shocks behind shock 3W, pointing similarly to minor fluctuations and faint internal shocks in the emerging jet.

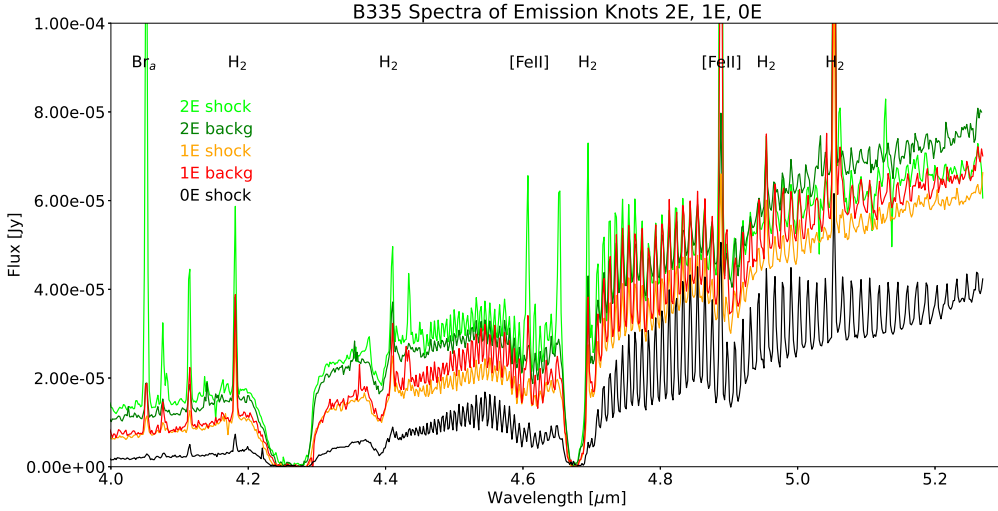


Figure 9. The spectra closest to the protostar in the eastern lobe of B335. Knot 0E, in particular, shows strong CO emission, but less H₂ and [Fe II] emission than the other knots. For shock 0E, background subtraction was not possible. For the other shocks, the nearby cavity background outside of the shock front itself, defined in Figure 8, is indicated with a similar, but darker color. CO emission is only slightly fainter, but certainly present, in those background positions outside of the shock front.

3.6.3. The Strong Shock 3E

Shock 3E (Figure 10) shows emission lines from shock-excited H₂ and [Fe II], but also very strong CO emission. Shock 3E, and also 2E, have some H₂ emission, but it is relatively weak compared to the shocks further downwind.

We conclude that shock 3E in Figure 10 itself is a pure emission line spectrum, and that the continuum contribution in its spectrum originates from the foreground and background in the outflow cavity.

The theory of atomic and molecular emission in, or behind, strong J-shocks has been developed by Hollenbach & McKee (1979), Hollenbach & McKee (1980), Hollenbach & McKee (1989). Comparable results were obtained in Orion by González-Alfonso et al. (2002). 3E is a very strong shock. [Fe II] emission is strong, and so is CO, indicating both an ionic component and high density in the molecular component of the shock. The [Fe II] emission is upwind from the H₂ emission, as is demonstrated in the color-coded difference image (Figure 15). Emission from H₂ is relatively weak. This is probably caused by H₂ dissociation in this strong shock. The [Fe II] emission in such a strong shock is further enhanced by grain sputtering in the high-temperature environment of the shock, increasing the Fe abundance in the gas phase. We interpret 3E, which has a kinematic age corresponding to the onset of the present photometric outburst, as the shock front between the hot and fast wind generated in this event and slower material ejected prior to that. The slower, older jet material is largely molecular. The spatial separation of [Fe II] emission and H₂ can be explained by H₂ being excited by the UV generated in the shock, before being dissociated by it.

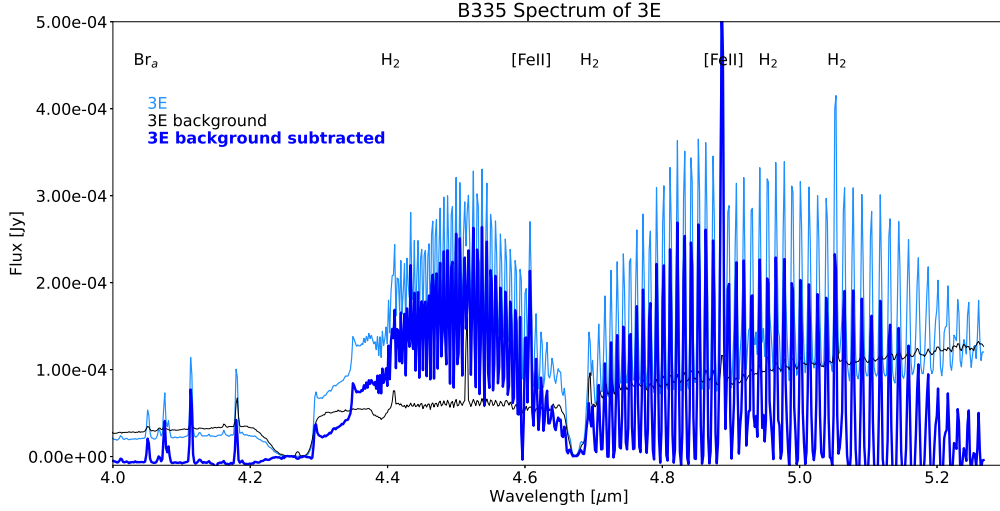


Figure 10. NIRSpec spectra of shock 3E. Light blue is the original spectrum at the position of 3E. Black is the spectrum in the nearby reference position showing mainly a continuum with ice absorption features, and dark blue is the background-subtracted, almost pure emission spectrum of shock 3E itself.

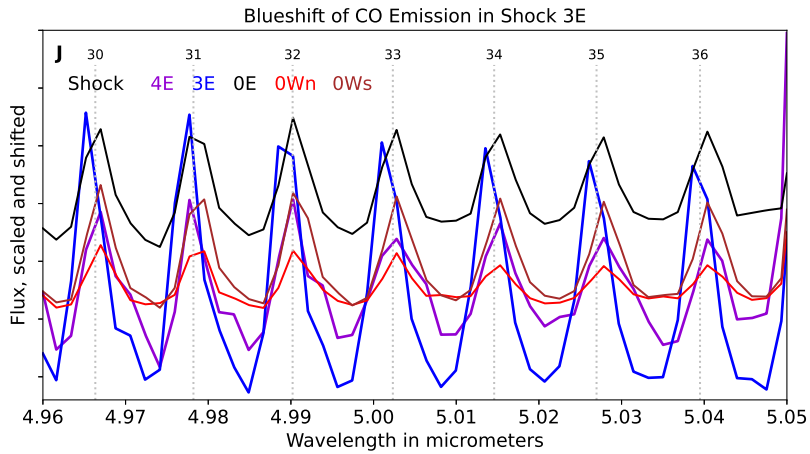


Figure 11. For different integration apertures, this figure shows spectra over a small wavelength range to illustrate the particular blue-shifted velocity of shock 3E. The spectra are in units of flux, but are both scaled and shifted for clarity. The CO emission lines in shock 3E (blue) are blue-shifted compared to the lines in the regions close to the protostar 0E (black), 0Wn (red), and 0Ws (brown). The older shock 4E is slightly blue-shifted relative to the shocks near to the protostar, but less so than shock 3E. The emission lines of shock 3E are blueshifted by 1.37 ± 0.07 nm, corresponding to a radial velocity of -84 km s^{-1} .

3.6.4. Shock 4E

For shock front 4E, only the southern component 4Ec was included in the NIRSpec data cube from program 1802. For shock front 4E, the cavity background was measured in a separate rectangular aperture from the aperture integrating over the 4Ec component. The result is very similar than for 3E: the cavity background continuum (black line in Figure 12) shows essentially no CO emission, and the spectrum of the shock is practically a pure emission line spectrum. Its spectrum confirms the much fainter CO emission, compared to shock front 3E, and the very strong H₂ emission lines. The spectrum of 4Ec shows a substantial continuum level, probably scattered continuum light from the protostar included in the integrating aperture. Shock 4E has very similar proper motion as shock 3E, which we interpret as the bulk motion of the central jet in the outflow, with the shocks being the result of perturbations in this flow. [Fe II] is very weak, this is a low velocity internal shock downwind from the point of interaction (shock 3E) of the strong, fast, and hot wind generated in the recent photometric event. Shock 4E represents material ejected by the protostar prior to the photometric event, shocking with slow relative velocity into even slower material ejected earlier. As mentioned earlier, a detailed analysis of the excitation conditions in each shock is not within the scope of this paper, and will be published separately.

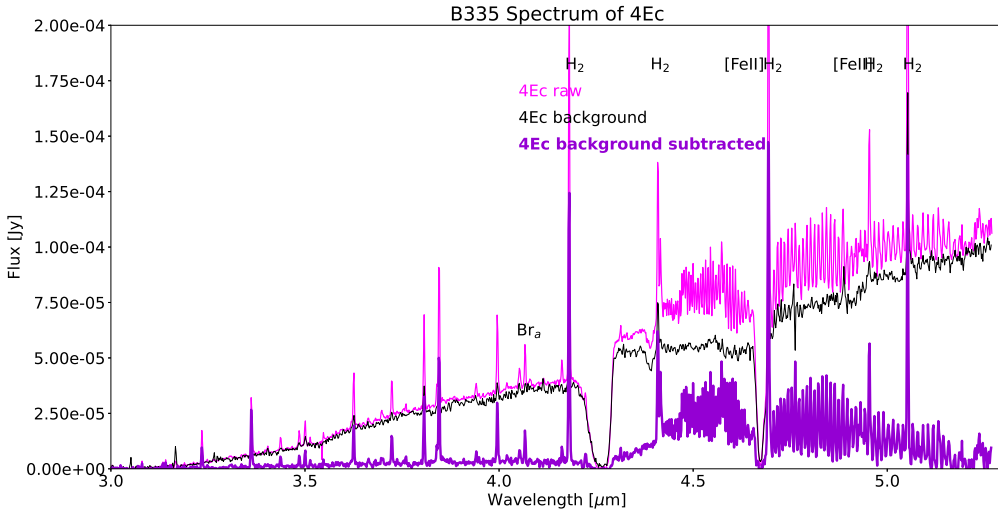


Figure 12. NIRSpec spectra of shock 4E. Light violet is the original spectrum at the position of 4E. Black is the spectrum in the nearby reference position, and dark violet is the background-subtracted, almost pure emission spectrum of shock 4E itself.

3.6.5. Knots 0Wn and 0Ws

To the west of the protostar position, there are two emission knots detected in the F444W filter. The southern of these knots, 0Ws, does not show a clear signature of proper motion in the difference image, and follows the rest of the outflow cavity reflection nebula in being fainter in 2024 than in 2023. This emission region shows complex morphological changes between our two epochs of imaging observations. Interpreted naively, these changes appear to be a strong apparent proper motion in a general direction towards SE, different from any of the other shock fronts. The radial velocity of this feature is close to the systemic velocity represented by shock 0E and very distinct from that of the jet shock fronts. With the information available, we cannot clearly identify this as a shock front, and favor an interpretation as a reflection nebula subject to locally changing illumination conditions. For this reason we do not list shock 0Ws in Table 1 and we do not show a proper motion vector in Figure 6. The northern knot (0Wn) also does not show motion, but has increased in brightness (i.e., appears white in the difference image).

We should point out that both 0Wn and 0Ws are much further away from the protostar than 0E. In fact, their separation in NS direction is similar to the opening of the outflow cavity at the same distance from the protostar in the eastern direction. The 0Ws region shows shock-excited features in its spectrum, including CO emission, similar to that seen in the 0E and 0Wn region.

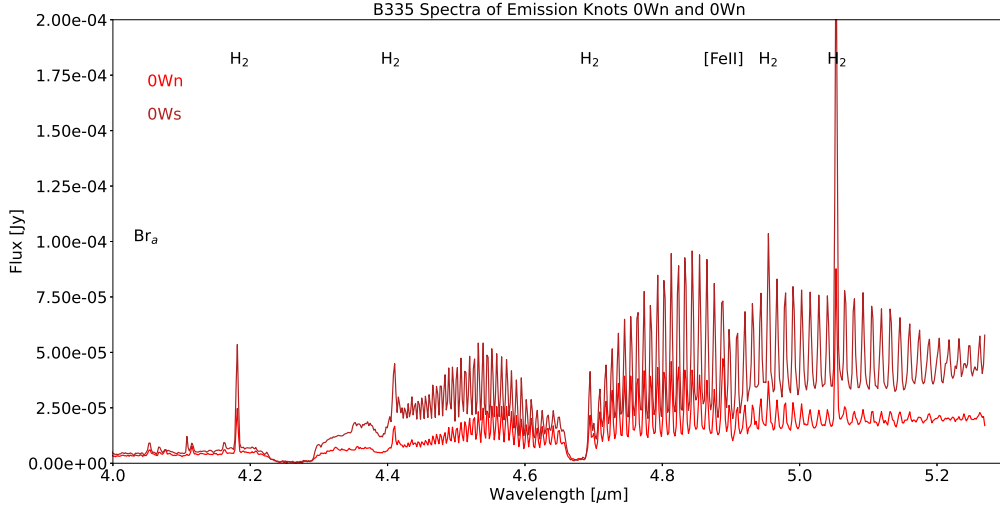


Figure 13. The western lobe of the outflow. Shock 0Ws (brown) appears to have higher CO excitation than 0Wn (red).

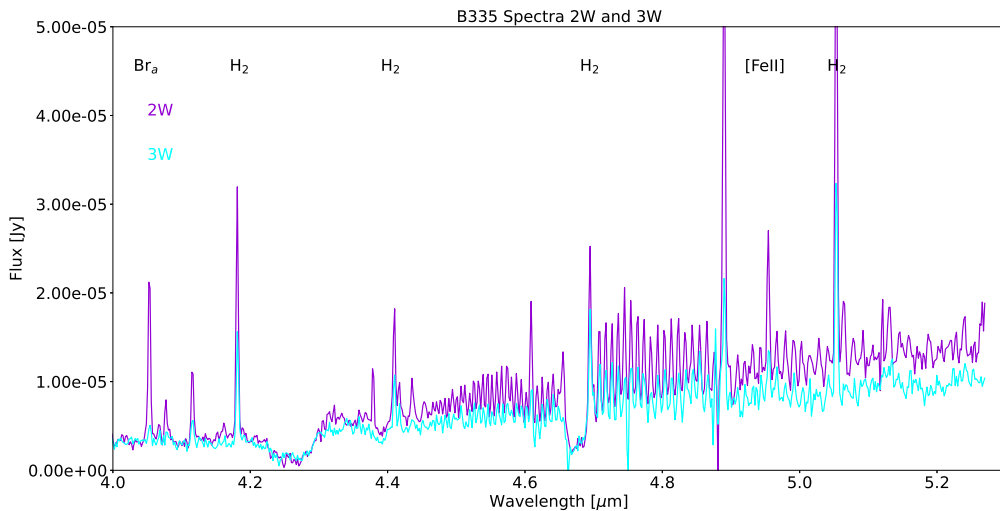


Figure 14. The western lobe of the outflow. Shock 2W (violet) and 3W (cyan) show relatively weak CO emission and are dominated by H₂ and [Fe II] emission lines. The tendency of decreasing CO emission with distance from the protostar is similar to the trend in the eastern lobe.

3.6.6. Shocks 2W and 3W

The two shock fronts 2W and 3W are only faintly indicated in the continuum image. The extracted spectra shown in Figure 14 reveal some CO emission, but are dominated by H₂ and [Fe II] emission lines. In the spectral images shown by Federman et al. (2024) shocks 2W and 3W appear as the western part of the [Fe II] jet. While the symmetric distribution around the protostar position and the similar proper motions in the east (blueshifted) and west (redshifted) outflow lobe strongly suggest that corresponding shocks were ejected at the same time, their excitation conditions are clearly not identical. While their spectra are similar to the minor shock 2E in the eastern lobe, they differ substantially from the shock front 3E, where CO emission dominates.

3.6.7. Diminishing Excitation along the Eastern Jet

For the extraction of line fluxes, and for the image cutouts in Figure 15, the continuum was calculated from a linear fit through the minima between the four adjacent CO lines, and subtracted from the spectra. We are using the strong H₂ (0,0) S(8) line at 5.053 μm and the fe II line at 4.889 μm because they are close together and extinction corrections between them are negligible for our purposes. At the spectral resolution of the NIRSpec data, both this [Fe II] and H₂ line are blended together with a CO emission line. We therefore subtracted the average line flux of the four adjacent CO lines from the raw integrated [Fe II] and H₂ line flux, to arrive at the line flux free of the contribution from the blended CO line. We are using this average of neighboring CO lines as a measurement of the CO emission line strength at the [Fe II] and H₂ lines and thus display two data points for the CO emission in Figure 15. Going from the immediate vicinity of the protostar (0E) to shock fronts farther away (2E, 3E, 4E) and beyond (5E and 7E, discussed in Paper I) there is a pattern of decreasing excitation going from the youngest shock fronts, 2E and 3E, towards 4E, 6E, and 7E, as was pointed out for the more distant shocks by Hodapp et al. 2024, based on slitless spectroscopy: while shock 3E shows CO and [Fe II] emission, the older shocks further downwind show predominately H₂ emission. This holds true even in those cases (3E and 4E) where we could subtract the flux contribution from the “cavity background”, which is dominated by H₂ emission. The same subtraction of a diffuse background is an unavoidable side effect of spectrum extraction in slitless spectroscopy used in Paper I.

A detailed analysis of the excitation conditions in each shock front is beyond the scope of this paper, and is being worked on for a separate publication. We only comment here on the line ratios in the four youngest shock fronts 0E through 4E in the eastern, blueshifted lobe of the B335 outflow on the basis of the 2022 NIRSpec data set.

Federman et al. (2024) have shown an extracted spectrum of the innermost region of the eastern outflow, larger than, but encompassing the shock defined as 0E here. This region shows a combination of H₂, CO, and [Fe II] emission, each of closely the same line flux. The region 0E is distinct from the other shock fronts. Its radial velocity is different from the main jet shock 3E and it does not show proper motion. We therefore interpret it as a combination of scattered light from the protostellar source itself, explaining the strong continuum, and shocks from a much slower disk wind. Shock 0E shows CO emission west of the starting point of the jet seen in Br α and [fe II] and the apex of the outflow cavity outlined in H₂ emission. This may be the first hint of a direct-line detection of the position of the protostar. The launch region of the jet traced in [fe II] is much narrower than the inner regions of the outflow cavity.

The shock 2E has a complex structure: The high-excitation tracers Br α and [fe II] roughly trace the central jet, as is already seen in the image in Federman et al. (2024). Emission by H₂ is faint and spatially anti-correlated with [fe II]. This may indicate that H₂ in this region is radiatively excited by UV from the hot regions of the 2E shock. Shock 2E is dominated by [fe II] and Br α emission, while molecular emission lines are much fainter, and are detected outside of the high-excitation shock front. This can be explained by destruction of the molecules in the hot shock front.

In the strong shock 3E, the position of the shock varies with the excitation of the emission line. The maximum of Br α is closest to the protostar, [fe II] and CO are a little further downstream, and H₂ peaks farthest downstream and is more extended. Overall, this shock is dominated by [fe II] and CO emission, while H₂ is faint. H₂ emission is found downstream from the high-excitation shock front, and may be excited by UV radiation from that shock.

Shock front 4E is dominated by H₂ emission, confirming that finding from Paper I, while the higher excitation lines are all fainter by an order of magnitude.

3.7. The Outflow Cavity Nebula

The B335 protostar is not directly detected (Stutz et al. 2008) at wavelengths up to 5.3 μm that we discuss here. In addition to the individual shock fronts discussed above, B335 is a bipolar nebula, with its eastern, blue-shifted lobe being more prominent. In the context of the variability of the B335 bipolar nebula, we have already established that the rapid variability and the local shadow effects indicate that a substantial fraction of the bipolar nebula is reflected light. The extracted line images in Federman et al. (2024) show that H₂ emission lines outline an outflow cavity that is broader than the jet, but narrower than the continuum reflection nebula.

The jet proper motion (shock 3E) shows that the outflow axis is close ($< 22^\circ$) to the plane of the sky, and the protostar is therefore seen through a nearly edge-on disk as we illustrate in the schematic cross-sectional sketch in Figure 17. In order to quantify the rapid increase of the extinction close to the protostar, we have selected a set of extraction apertures in the blue-shifted outflow cavity that are not associated with any shock fronts or shock-excited emission knots and identify them in Figure 16 superposed on an image extracted from the NIRSPEC data cube, in colors matching those used for the spectra in the following figures. Position 0 is identical to shock front 0E, which we

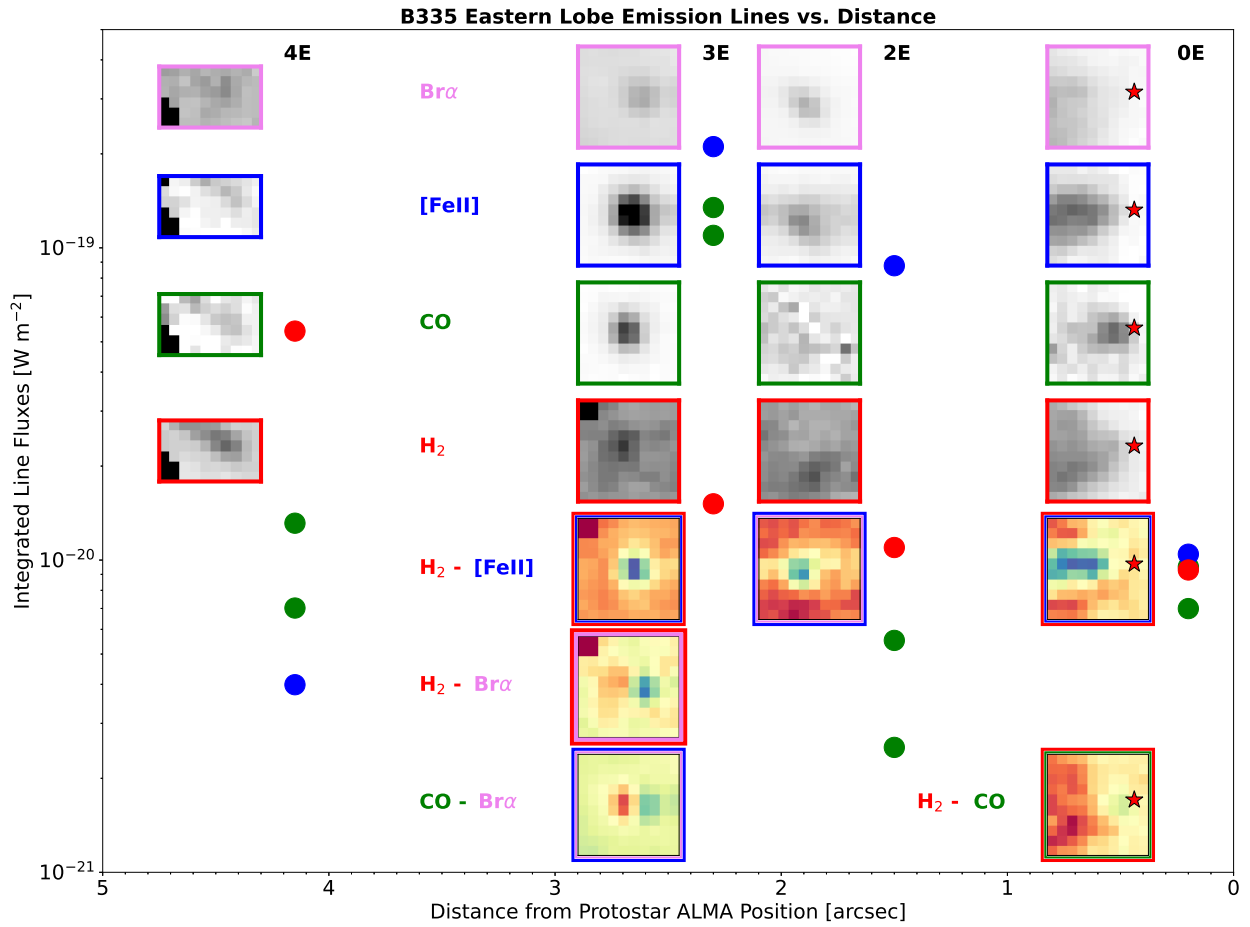


Figure 15. This figure shows both the line flux as large circles and the spatial distribution of the line flux as small image cutouts, for the four innermost shock regions in B335: 0E, 2E, 3E, and 4E. The color coding, both for the line flux symbols and for the image frames, is [Fe II] (blue), CO (green) adjacent to the [Fe II] and H₂ lines, and H₂ (red) lines. The x-axis shows the distance from the ALMA position of the protostar, from right to left, so that the inserted cutout images have the proper orientation relative to the axis. The inserted cutouts are integrated intensities over the these lines after subtraction of the continuum and of overlapping CO lines. Their vertical arrangement is in order of wavelength, and has no relationship to the flux scale. We also include Br α at 4.052 μ m as image cutouts, but do not plot line fluxes, since its wavelength is shorter than those of the other lines and extinction corrections would be substantial and are not precisely known. We show some difference images in colored intensity scaling to document that high-excitation atomic and ionic lines in the jet are emitted at different locations than relatively low-excitation molecular lines showing the structure of excitation conditions within each shock front.

have determined not to be part of the jet, on the basis of its low proper motion and different radial velocity. Positions 1 and 2 are at the same distance from the protostar as shock fronts 1E and 2E, but are north of those shock fronts and in general, are away from the jet axis. Cavity positions 1 and 2 still show CO bandhead emission, but with decreasing strength. Cavity positions C3 and C4 (yellow), are away from the jet axis, at distances slightly closer to the protostar than shock 3E. Cavity positions C5, C6, and C7 (green) are removed from individual shock fronts at a distance larger than shock 3E. The combined spectral traces in yellow show very little CO emission, while the green averaged spectrum shows essentially none. All these cavity positions show H₂ emission lines, with diminishing strength with increasing distance. We conclude that the CO lines detected in the area of the cavity, away from individual shock

fronts, are produced by the slower disk wind that also produces the H₂ emission. These lines are not simply reflected light from the immediate surrounding of the protostar, which should produce a similar spectrum of the reflected light, independent of distance.

At the positions closest to the protostar, we observe dominant CO emission in the spectrum of position 0E. In 1E and 2E, the CO lines are roughly equally strong in the jet than in adjacent “background” positions. The CO lines at these positions are not emitted in the jet, but in a wider outflow cone of similar opening angle to the H₂ emission cone. In those positions (1E and 2E), the ratio of continuum to CO has strongly shifted towards more continuum, the latter being mostly scattered light from the immediate surroundings of the protostar.

Other than those lines, the cavity spectra show a strong continuum component. This is mostly reflected light based on the shadow effects and the variability. A strong contribution from local thermal continuum emission from dust heated in or near the region of H₂ shock emission could not explain the rapid variability of the flux.

At the distance from the protostar of shocks 3E and 4W, the “background” positions away from the jet do not show CO emission, but the shock positions have strong CO emission, which therefore must have been produced in those shock.

To summarize the distribution of gaseous CO emission: CO dominates at the closest position to the protostar where we have data from. In the 1E and 2E positions, a strong continuum with a weaker component of CO emission is observed. Still farther from the protostar, positions away from the jet show hardly any CO emission, while shock 3E, in particular, shows very strong CO generated in this shock itself. Since the ration of continuum to CO emission changes drastically within 3 arcsec from the protostar, not both of them can be the same scattered light. Since CO R and P band emission is associated with higher temperatures than continuum emission, we believe the CO emission outside of shock fronts is scattered light from the immediate surroundings of the protostar, while the continuum is emission from the walls of the outflow cavity.

3.7.1. *Extinction in front of the Reflection Nebula*

The NIRSpec IFU spectra integrated over these extraction apertures are shown in Figure 18. Since we are interested in the shape of the continuum spectrum, and not in the absolute flux, we normalize all spectra to unity at an effective wavelength of 3.92 μm . For clarity, the spectra are color coded in the same way as the apertures in Figure 16, in a wavelength sequence of color going from violet for the most distant to brown and black for the closest extraction apertures. It is clear from Figure 18 that the spectra are much steeper closer to the protostar. The spectra closest to the protostar show strong CO emission around 5 μm on top of a continuum spectrum. We use the minimum flux between a set of five CO emission lines at an effective wavelength of 5.09 μm as a measure of the continuum flux in this region. The continuum points extracted this way are shown as open circles in Figure 18. From the flux ratio between 5.09 and 3.92 μm we compute the A_V using the infrared extinction law by [Wang & Chen \(2019\)](#). The results are nominal extinction values that incorrectly assume a flat spectrum of the protostar illumination. However, it is a reasonable approximation that the spectral energy distribution of the light emerging from the protostar and then illuminating the outflow cavity is the same for all positions in the cavity and therefore is the same each of the extraction apertures. Relative extinction values between the different apertures can therefore be determined with better certainty. We measure an increase of extinction by $A_V = 250$ mag from the most distant extraction aperture 3.''5 from the protostar to the closest, 0.''2 from it. A caveat and the reason for stating this as an approximation is that we have evidence for local and time-variable absorption effects from the time variability of the cavity flux shown in Figures 6 and 7.

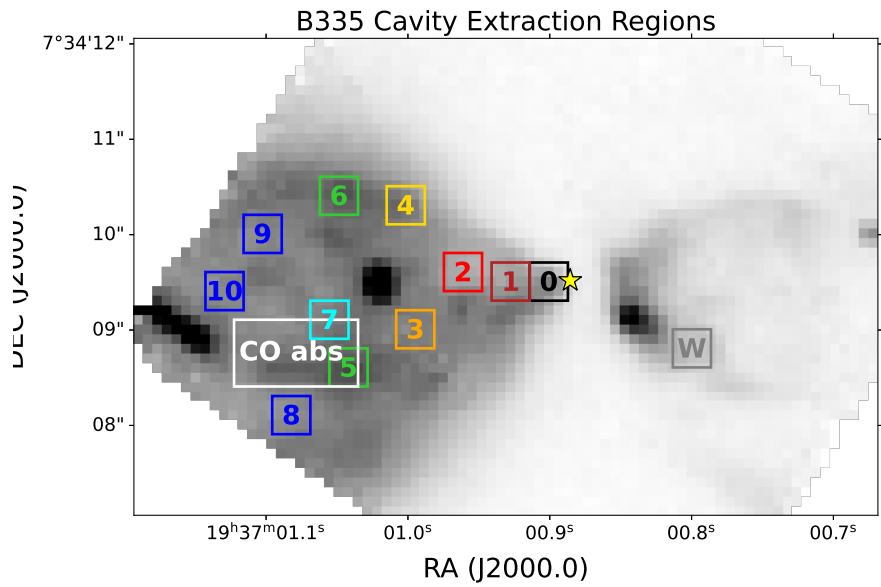


Figure 16. Extraction apertures in the reflection nebula other than shock fronts. The image is the NIRSpec IFU data cube slice at a wavelength of $5.053 \mu\text{m}$, centered on an H_2 emission line. The extraction boxes are color coded (blue-green-yellow-red-brown-black) in a sequence suggesting increasing extinction, consistent with the coloring of the spectra in Figure 18. The regions in yellowish, greenish, and blue will be averaged for the spectra in Figure 18, to improve the S/N ratio. The white rectangle indicates the extraction region where we found CO gas absorption. All other regions show CO in emission. The position of the protostar at the epoch of the NIRSpec observations is indicated by a yellow star symbol.

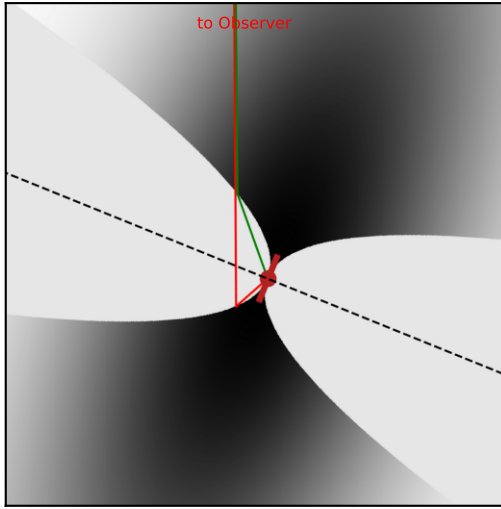


Figure 17. A schematic cross-section illustrating the scattering geometry for light scattered on the outflow cavity walls, and then suffering extinction in the outer regions of the flattened molecular core surrounding the protostar. The direction toward the observer is vertically to the top. The scattered light in the blue-shifted cavity does not pass through the equatorial plane of this flattened molecular core, nor through any protoplanetary disk surrounding the protostar, the latter being schematically indicated in brown color. The jet axis of the outflow near the symmetry axis of the outflow cavities is indicated as a dashed line.

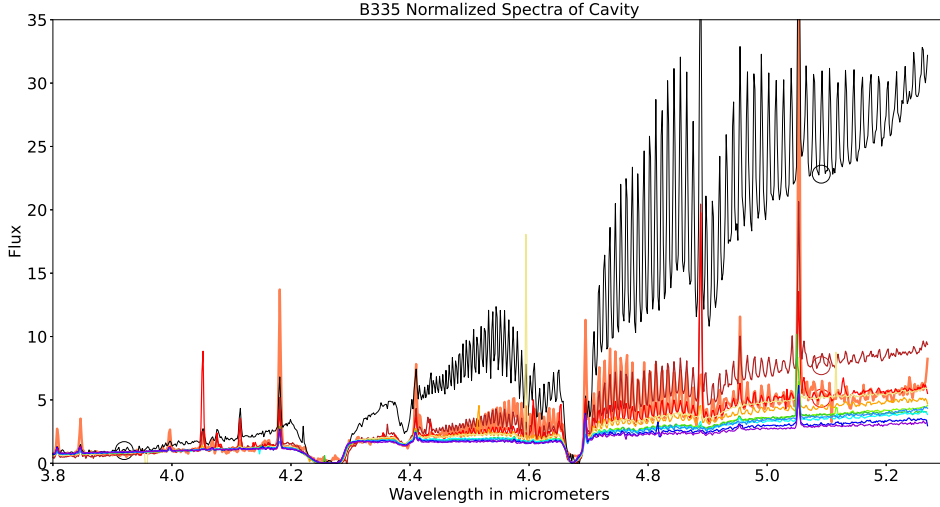


Figure 18. The spectra extracted from the reflection nebula positions (Figure 16) outside of known jet shock fronts were normalized in an emission line free region from 3.86 to $3.98\ \mu\text{m}$, indicated by an open circle. The spectra show strong, saturated ice absorption features of $^{12}\text{CO}_2$ and ^{12}CO , and the non-saturated feature of $^{13}\text{CO}_2$. Closest to the protostar, in particular in Knot 0E, the spectrum is dominated by strong CO gas emission. The overall slope of the spectra indicates rapidly increasing extinction close to the protostar.

We have extracted continuum spectra of the cavity positions defined in Figure 16 by using the minima between the individual CO emission lines as a measure of the continuum. We are going to refer to this spectrum as the CO-line-minimum spectrum. This procedure uses only a fraction of the data points in the original spectra, and therefore is undersampling narrow emission lines. However, the broad absorption features of ices are adequately sampled. We extracted this continuum and ice absorption spectrum for each of the cavity positions. For clarity of presentation, and illustrated in Figure 19, we have averaged the spectra in cavity positions 3 and 4, the result being shown in red in Figure 20 cavity positions 5, 6, and 7, the result being shown in green, and positions 8, 9, and 10, the result being shown in blue. For wavelengths below $4.4\ \mu\text{m}$, we show the normalized spectra in their original sampling, since there are only a few well separated emission lines in this wavelength range. The cavity position numbers correspond to increasing distance from the protostar and the color coding in Figures 18, 19, 20, and 21 is intended to suggest increasing extinction. All the spectra in Figure 20 were normalized by the median of the CO-line-minimum spectrum between 4.45 and $4.55\ \mu\text{m}$. We again note the trend of decreasing slope of the continuum with distance from the protostar. We also note that all ice absorption features shown here become more shallow with increasing distance.

3.7.2. Ice Absorption

Figure 20 shows that the absorption features of $^{12}\text{CO}_2$ and ^{12}CO ice are strong and saturated in all outflow cavity positions. $^{13}\text{CO}_2$, OCN^- (cyanate anion) and OCS (carbonyl sulfide) ices are convincingly detected and their depths increase towards the protostar. ^{13}CO ice is weakly detected, and the broad absorption of HDO ice at $4.1\ \mu\text{m}$ (Slavicinska et al. 2024) tentatively in the spectrum of region 0E, the position closest to the protostar. The continuum emission declines strongly at shorter wavelengths, and that portion in Figure 20 (enhanced by a factor of 20 for clarity) shows that the absorption feature of the C-H stretch mode is detected in the three cavity positions farther away from the protostar ($>1''$). In the context of YSOs, this C-H stretch signature is commonly identified as CH_3OH , laboratory spectra of which were shown in Dawes et al. (2016), but our data are of insufficient quality to support this specific identification. Finally, while the NIRSpec data cubes cover the wavelength range of the broad H_2O ice feature near $3.0\ \mu\text{m}$, no usable data were obtained of this feature due to the high column density and saturation of the absorption as well as the faint continuum.

For all these ice features, we computed optical depth spectra relative to a local continuum and determined integrated optical depths (in units of cm^{-1}). The resulting integrals were divided by the integrated laboratory band strengths (A) to give column densities in units of molecules cm^{-2} . We used the A -values from Bouilloud et al. (2015) for $^{13}\text{CO}_2$.

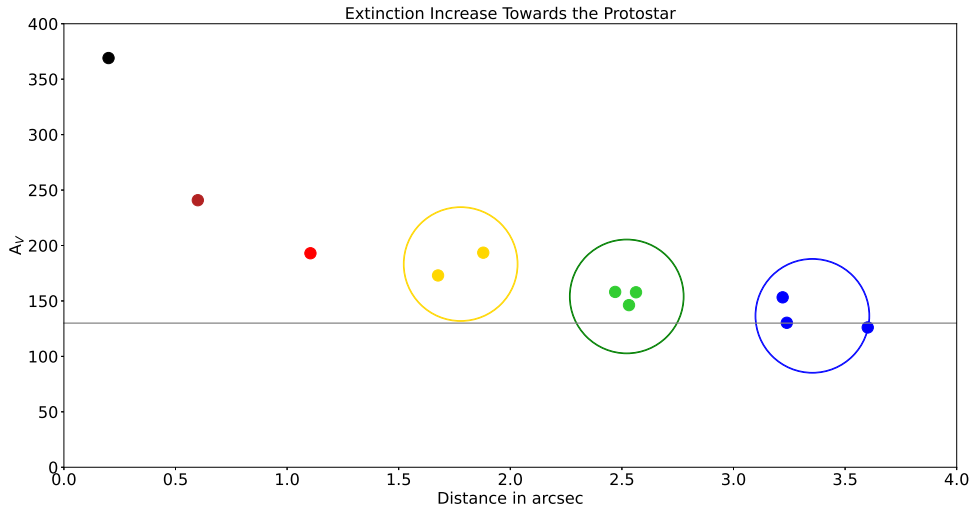


Figure 19. Plot of the A_V in the selected apertures in the blue-shifted outflow cavity walls (Figure 16), dependent on the distance from the protostar. The extinction was determined from the normalized spectra in Figure 20 between intervals at effective wavelengths 3.92 and 5.09 μm indicated by open black circles. At the long wavelength point, the minima in the CO line forest were assumed to represent the continuum. While the illuminating spectrum from the protostar is unknown, the assumption is that every point in the reflection nebula is illuminated by the same spectrum, i.e., that the extinction in the outflow cavity is negligible. Therefore, while the absolute value of the extinction is uncertain, the increase with position towards the protostar can be measured. The line at a level of $A_V = 130$ indicates the baseline at a distance of $3.5''$ from the protostar. Therefore, we measure an increase of extinction of about 200 magnitudes of A_V from that position to the closest observed feature near the protostar. We also indicate the groups of positions that were averaged for the analysis of the ice features by large circles, with their color corresponding to the ice absorption spectra in Figure 20.

For OCN[−] we used $A = 1.51 \times 10^{-16}$ from Gerakines et al. (2025), and for OCS 1.20×10^{-16} from Slavičinská et al. (2025).

The NIRSpec data cube was used to produce ice band optical depth maps across the entire outflow cavity (Figure 22) and also to study the ice band profiles at specific positions in more detail (Figure 20). The spatial distribution of the ice band optical depths as well as the continuum extinction are shown in Figure 22 on a per-pixel basis. We omitted the area of the strong shock 3E from the discussion because it is dominated by gas emission lines and the derived optical depths are unreliable. Two general trends are visible. First, the ice absorption and dust extinction strongly increase towards the protostar, as the line of sight passes through denser regions in the flattened molecular core, as schematically illustrated in Figure 17. And second, it is apparent that the absorption is concentrated outside of the outflow cavity. To highlight this spatial relationship, we show an image of the shock-excited H₂ emission generated at the interface between the outflow cavity and the ambient molecular core material. We conclude that the outflow cavity shows less absorption both in continuum dust extinction and in specific ice features compared to the surrounding molecular core, indicating a reduced dust density in the outflow. This is consistent with the results in Figures 3 and 4 from the photometric H₂O ice column density maps on larger spatial scales, and the appearance of the outflow cavity in the scattered light (coreshine) images in 1. Put together, three largely independent methods indicate that the outflow cavity has lower dust extinction and lower absorption in all our observed ice features: background star photometry, scattered light imaging at large distances, and scattered light spectroscopy on short distances from the protostar. We believe this is due to the higher temperature of the outflowing gas, compared to the ambient molecular core material, both from its launch conditions near the protostar and continual heating from shocks. Under such elevated temperatures, dust, and certainly its ice mantles, are destroyed during outflow launch, and will not recondense in the outflow cavity.

The absorption feature of $^{12}\text{CO}_2$ near 4.27 μm is saturated in all the spectra recorded here (Figure 20), but the long-wavelength wing strength depends on the distance from the protostar and therefore on total extinction. The position closest to the protostar appears to show some evidence of the scattering peak short of the saturated $^{12}\text{CO}_2$

feature as well. These wings of the $^{12}\text{CO}_2$ ice feature have been modeled by Dartois et al. (2022) as scattering by dust mixtures containing grains of up to several micrometers in size, and thus they are evidence of grain growth in dense environments. Both the short and long-wavelength wings have been observed in other protostellar sources. Of the sources discussed by Dartois et al. (2022), NGC7538 IRS9 has the strongest features, but these are not as pronounced as in the B335 lines of sight.

The ^{12}CO ice feature near $4.67\text{ }\mu\text{m}$ is saturated closest to the protostar, but appears to just come out of saturation for the less obscured lines of sight (Figure 20). From the scattering models in Dartois et al. (2022), asymmetries between the short and long wavelength wings of the main absorption are expected here as well. However, blending with other ice features (OCN^- , CO mixed with polar molecules) complicates detections of these possible scattering asymmetries.

The $^{13}\text{CO}_2$ ice feature is not saturated in any of our spectra, and its depth is strongly dependent on the distance to the central star. Based on the same data, Brunken et al. (2024) presented a detailed analysis of the $^{13}\text{CO}_2$ feature in a larger aperture centered on the protostellar position, i.e., comprising features 0E, 0Wn, and 0Ws in our terminology. They find that the strongest absorption component is from $^{13}\text{CO}_2$ mixed with H_2O , followed by $^{13}\text{CO}_2$ mixed with CH_3OH , with minor contributions from $^{13}\text{CO}_2$ mixed with CO of two different temperatures (15K and 25K), and finally a very small contribution from pure $^{13}\text{CO}_2$ at 80K. Given the viewing geometry where the protostar itself is behind a close to edge-on disk, it is not surprising to find contributions from ices with a substantial range of temperatures.

As is shown in Appendix C, the strong detection of the OCS and OCN^- ice absorption bands against the scattered continuum emission allows for a detailed study of the ice band profiles across the B335 outflow cavity. The analysis of the CO ice band is limited by it being saturated. The OCS band has a Gaussian peak position and FWHM of $4.900 \pm 0.008\text{ }\mu\text{m}$ and $0.04 \pm 0.01\text{ }\mu\text{m}$, respectively, for all extracted positions across the cavities. This is comparable to the bulk of the massive YSO targets studied in Figure 13 of Boogert et al. (2022), and consistent with OCS embedded in CH_3OH -rich ices, and proton-irradiated H_2S - or SO_2 -containing ices. While the column densities increase towards the protostar (Figures 20 and 21), the OCN^-/OCS column density ratio is constant across the outflow cavities, with a mean of 4.0 and a standard deviation of 0.4 (see also Figure 21). This is $\sim 50\%$ lower compared to massive YSOs (Boogert et al. 2022). Overall, other than column densities, the ice characteristics seem to depend little on the varying conditions in the B335 environment, and mildly at most when compared to deeply embedded massive YSOs with orders of magnitude larger luminosities. An astrochemical discussion of the origin of these similarities and differences is beyond the scope of this paper. Although, the lack of strong signals of ice processing by the protostellar radiation (such as strong crystalline $^{13}\text{CO}_2$ ice and a weak feature of solid CO, the most volatile ice) is likely because most absorption is seen against light scattered out of the outflow cavities and then traces substantial column densities of dust and ice from the dense envelope, which overwhelms regions of highly processed dust mantles that may exist in the immediate vicinity of the protostar (Figure 17).

3.7.3. CO Gas Emission and Absorption

All the positions in the B335 outflow cavity show CO gas lines, in general with diminishing amplitude with increasing distance from the protostar. The spectra shown here were obtained with the NIRSpec G395M medium resolution grating, resulting in a spectra resolution of just above 1000 in the spectral region discussed here. At higher spectral resolutions, e.g., in the observations of GSS 30 by Pontoppidan et al. (2002), CO emission lines appear as narrow lines above a well-defined continuum. In the NIRSpec B335 data, as a consequence of this relatively low spectral resolution, the CO line spectrum appears as a near symmetrical oscillation of the flux, with emission and absorption not being immediately distinguishable. Wavelengths and identifications of the CO lines were taken from the HITRAN/HITEMP database, which uses the data from Goorvitch (1994). The radial velocity of the B335 molecular core relative to LSR is 8.34 km s^{-1} (Yen et al. 2015). With the kinematic correction applicable to the NIRSPEC observations, lines appear blueshifted by $\approx 20\text{ km s}^{-1}$ relative to the laboratory wavelengths indicated in Figure 23. We compare the CO gas spectrum of two regions close to the protostar (0E and 2E) with the average of a larger area away from the jet axis, at a distance between that of shocks 3E and 4E, indicated by a white rectangle in Figure 23. In this area, we note a phase shift in the R-branch (short wavelengths) lines, indicating absorption. In the P-branch, the situation is more complex, with lines of J-values between 13 and 28 appearing in absorption, while the other J values are in emission, i.e., in phase with the emission from regions 0E and 2E (black and red in Figure 23). We map the distribution of CO line absorption in Figure 24. Within the field of view of the NIRSpec data, the absorption is confined to the more

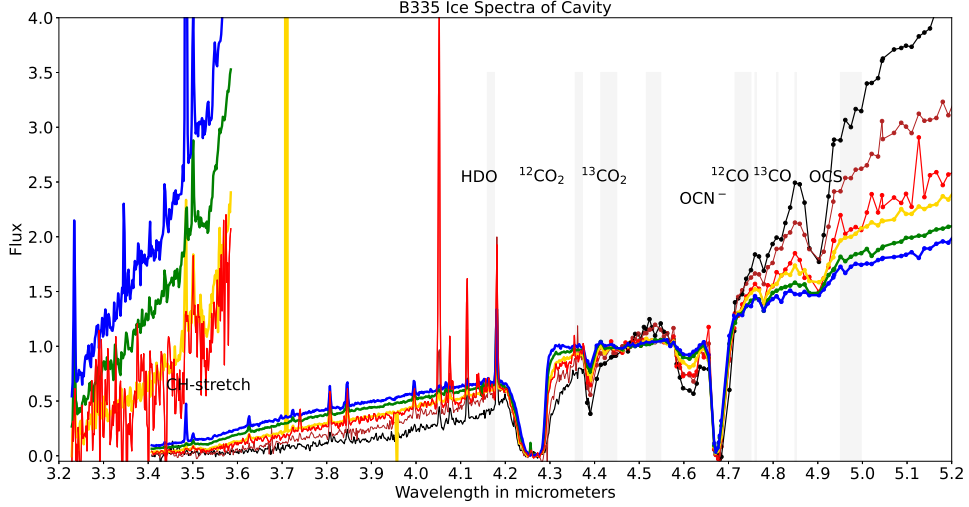


Figure 20. The spectra extracted from the reflection nebula positions (Figure 16) outside of known shock fronts were normalized in an emission line free region from 4.45 to 4.47 μm . For wavelengths longer than 4.4 μm , where CO gas emission bands are strong, the continuum spectrum was approximated by interpolating through the minima between CO lines, leading effectively to a reduced spectral resolution that was, however, still adequate to show the broad ice absorption features. Averaged spectra from several extraction positions are indicated by thicker lines. The band of H_2O ($\sim 3.0\ \mu\text{m}$) is saturated and marks the lower limit of useful data. At the short wavelength end, we show the same data expanded by a factor 20 to bring out the faint signature of the C-H stretch at 3.53 μm . CO_2 ($\sim 4.27\ \mu\text{m}$) ice is saturated at all positions, as is the CO ice band ($\sim 4.67\ \mu\text{m}$). The weaker ice features of OCN^- ($\sim 4.60\ \mu\text{m}$), OCS ($\sim 4.90\ \mu\text{m}$), $^{13}\text{CO}_2$ ($\sim 4.38\ \mu\text{m}$), and ^{13}CO ($\sim 4.78\ \mu\text{m}$) are not saturated.

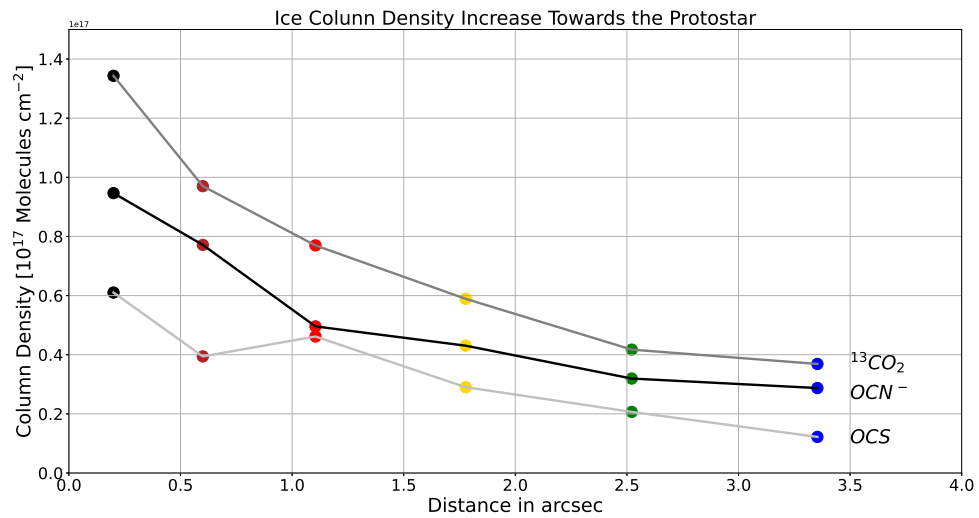


Figure 21. Ice column density vs. distance from protostar for three ice species $^{13}\text{CO}_2$, OCN^- , and OCS that are not saturated in the B335 cavity and have sufficient strength for a significant detection.

distant regions of the blue-shifted lobe, but within the outflow cavity defined by shock-excited H_2 emission, shown by Federman et al. (2024).

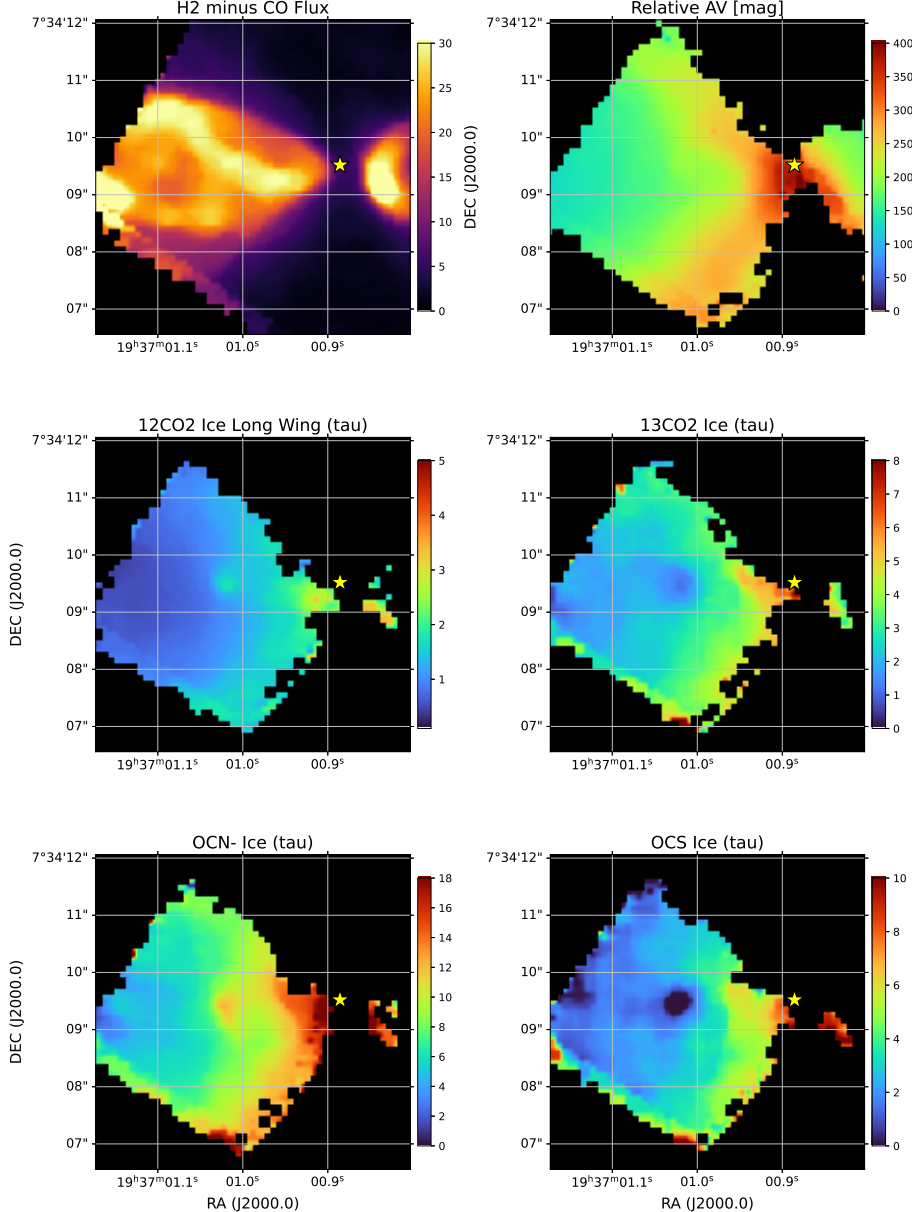


Figure 22. Maps of the dust absorption near the B335 protostar based on the NIRSpec IFU data cube. The top left panel is a flux image of shock-excited H₂ emission, corrected for CO gas emission. It shows the shocked interface between the outflow cone and the surrounding molecular cloud material and is used for comparison with the dust absorption maps. The top right panel shows the continuum extinction in the scattering path in units of A_V, with an unknown contribution from the color of the protostar light, as explained in the text. The lower four panels show the distribution of the optical depth in the scattering path for the ¹²CO₂ long-wavelength wing, the ¹²CO₂ feature, and the OCN- and OCS features. In all panels, the position of the strong shock 3E is standing out. Due to the very strong line emission in this shock, the data at this position are not reliable. Near the limits of the outflow cavity, the fluxes are very low and the extracted ice optical depths are therefore very uncertain. In particular, while we show the map in its entirety, we do not believe features on the jet axis can be trusted. All absorption features show a general trend of more absorption closer to the protostar, and stronger absorption in an envelope outside the H₂ emission cone, and less absorption in this cone itself.

We have now obtained new NIRSpec IFU data with the G395H grating, that have about double the spectral resolution of the data analyzed here, and we will, in the near future, revisit the CO gas emission and absorption with the goal of studying the temporal evolution of the gas emission.

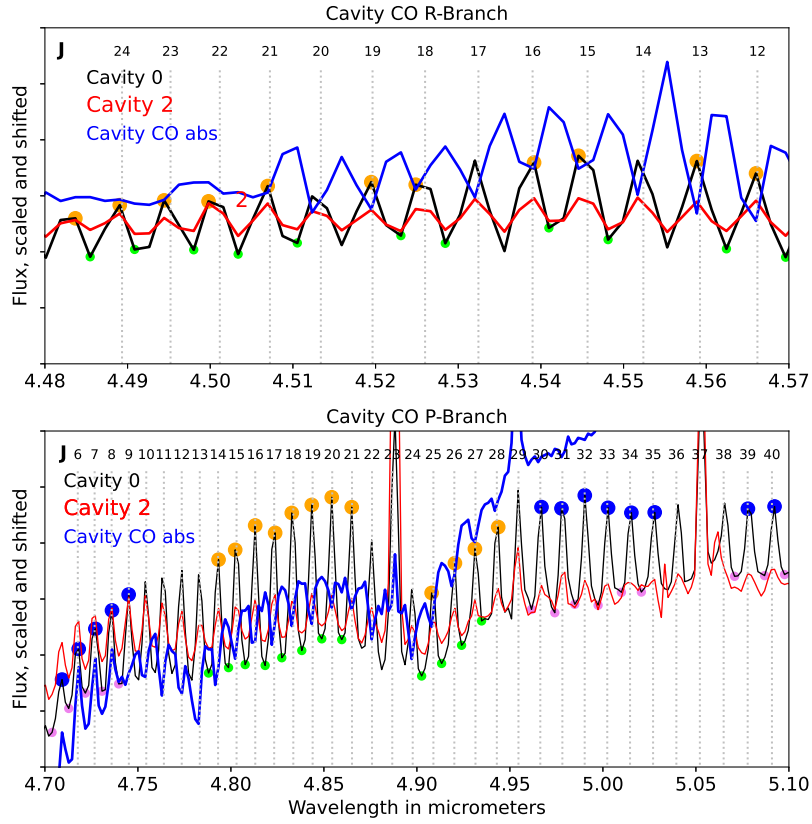


Figure 23. For different integration apertures, this figure shows spectra over a small wavelength range to illustrate both the CO emission and CO absorption in different regions of the outflow cavity. The spectra are in units of flux, but are both scaled and shifted for clarity. The CO line laboratory wavelengths are labelled with their J-number and indicated by dotted lines. Top Panel: CO R-branch emission and absorption. Bottom Panel: CO P-branch emission and absorption. Large orange circles indicate CO lines where absorption is observed in the “CO abs” position and that were used in the mapping of the absorption. In the bottom panel, blue circles indicate CO lines where no absorption was observed.

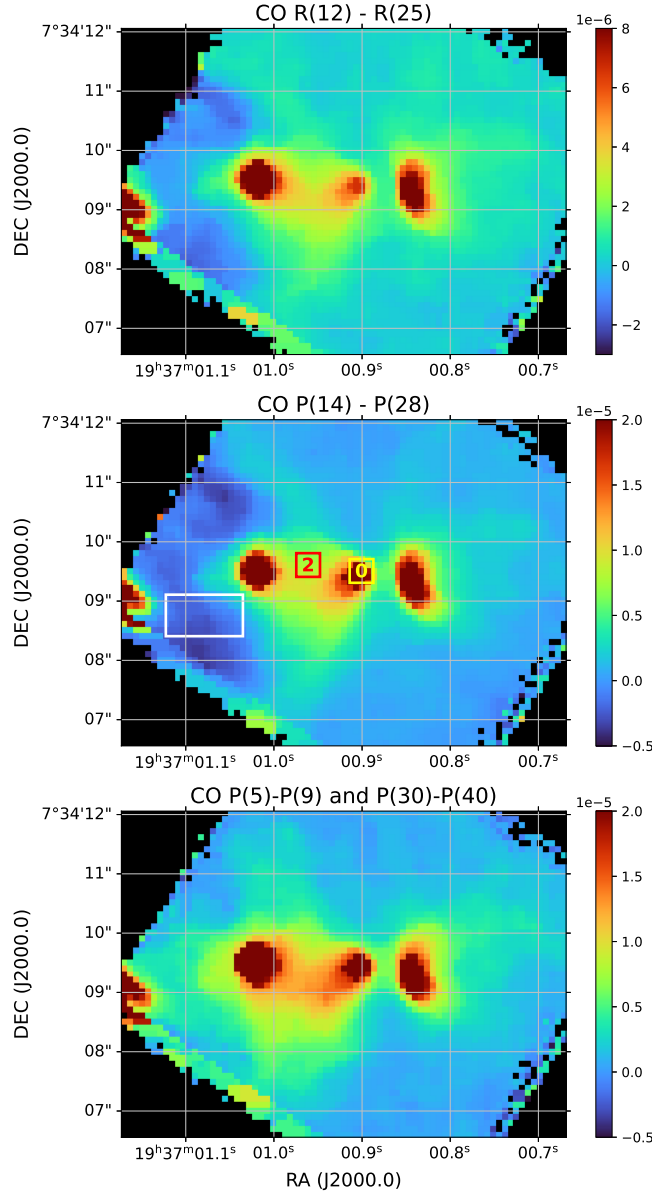


Figure 24. Maps of CO emission in the R and P branches. Red to brown indicates position difference signal, i.e., emission in CO lines. Violet to blue indicates negative difference signal, i.e., absorption.

4. SUMMARY AND CONCLUSIONS

We have analyzed two sets of JWST NIRCam images of the isolated globule B335 and the single protostar it contains. We also present new analysis of public JWST NIRSpec IFU data of the region closest to the protostar.

Based on NEOWISE photometry of the integrated light in the reflection nebula, the B335 protostar underwent a photometric outburst around 2015 and is at present in the declining brightness phase of this outburst, but has not yet returned to its quiescent brightness. In addition to the overall decline of brightness of the blue-shifted, eastern lobe of the reflection nebula, shadow effects from obscuring clumps in the path of the illuminating radiation from the protostar are projected into the reflection nebula. From the fact that substantial variations in these shadow effects are seen in the one year epoch difference between our two images, we conclude that those obscuring clumps must be of order one AU from the protostar. From the amplitude of the variations, we estimate that those clumps have optical depths of order unity.

A set of shock-excited emission knots near the center of the outflow cavity outlines a fast jet emanating from the protostar. Based on our astrometry of the individual shock fronts, their kinematic ages are short, of order of decades. The kinematic age of shock 3E, the brightest and most compact shock, is consistent with it having been launched in the early phases of the presently on-going photometric outburst. This shock front 3E is remarkable for the strong CO gas emission. The excitation of the shock fronts along the fast jet indicate that the present outburst of the protostar has produced a fast, hot, largely atomic jet. Shock 3E is the shock front where this jet is shocking against previously ejected slower gas leading to highly excited emission and a distinct blue-shifted radial velocity, probably due to lateral ejection of material from the shock. Shocks further downwind (4E and older) show rapidly decreasing levels of CO emission, and become dominated by H₂ emission. The kinematic ejection date of the complex shock front 4E is consistent with its ejection in a previous photometric outburst which is tentatively indicated by one Spitzer observation. The emission knots closest to the ALMA position of the protostar, in particular 0E, are not part of the fast jet, but are stationary shocks or slower moving disk wind features.

We present maps of the column densities of H₂O ice and continuum extinction based on NIRCam photometry of background stars and confirm the overall flattened structure of the B335 core, and the carving out of an outflow cavity that contains less dust and ice than the undisturbed molecular core. A study of the scattered interstellar radiation field, the coreshine, qualitatively confirms these findings and extends them to regions of lower density.

We study the spectra at selected positions in the blue-shifted outflow cavity that are not part of the jet. The continuum slope indicates rapid increase of the extinction toward the protostar, with an increase of approximately A_V = 200 mag in the inner 4'' towards the protostar, which establishes a lower limit for the total extinction towards the protostar. In the 4–5 μ m region, these scattered light spectra are dominated by ice features: ¹²CO₂ and ¹²CO are in deep saturation, and both show evidence of short and long-wavelength wings in their profile, indicating a contribution from larger grains. The rarer isotopologues ¹³CO₂ and ¹³CO are detected without saturation, as are OCN[−] and OCS. The features of ¹³CO₂, OCN[−], and OCS show strongly increasing optical depth towards the protostar, but no evidence of further chemical evolution closer to the protostar.

We have studied the emission of gaseous CO in the bipolar nebula associated with B335 and find that close to the protostar, CO is in emission, with low radial velocities, consistent with the systemic velocity of the B335 molecular core. CO emission is strongly blue-shifted in the jet shock fronts, in particular the strong young shock front 3E. We find CO absorption at distances from the protostar beyond the position of Shock 3E.

This project was supported by NASA through the JWST/NIRCam project, contract No. NAS5-02105 (M. Rieke, University of Arizona, PI). We thank the members of the NIRCam team for their work in designing, building, testing, and commissioning of the NIRCam instrument. This work is largely based on observations made with the NASA/ESA/CSA James Webb Space Telescope. The data were obtained under GTO program 1187 and GO program 1802 and downloaded from the Mikulski Archive for Space Telescopes (MAST) at the Space Telescope Science Institute, which is operated by the Association of Universities for Research in Astronomy, Inc., under NASA contract NAS 5-03127 for JWST. We thank Fengwu Sun for the use of his astrometrically re-calibrated NIRCam images. D.J. is supported by NRC Canada and by an NSERC Discovery Grant. This publication makes use of data products from the Near-Earth Object Wide-field Infrared Survey Explorer (NEOWISE), which is a joint project of the Jet Propulsion Laboratory/California Institute of Technology and the University of California, Los Angeles. NEOWISE is funded by the National Aeronautics and Space Administration. This research has made use of the NASA/IPAC Infrared Science Archive, which is funded by the National Aeronautics and Space Administration and operated by the California Institute of Technology. This work is based in part on observations made with the Spitzer Space Telescope, which was operated by the Jet Propulsion Laboratory, California Institute of Technology under a contract with NASA. ALMA is a partnership of ESO (representing its member states), NSF (USA) and NINS (Japan), together with NRC (Canada), MOST and ASIAA (Taiwan), and KASI (Republic of Korea), in cooperation with the Republic of Chile. The Joint ALMA Observatory is operated by ESO, AUI/NRAO and NAOJ. The National Radio Astronomy Observatory is a facility of the National Science Foundation operated under cooperative agreement by Associated Universities, Inc. This work is based in part on observations made with the Spitzer Space Telescope, which was operated by the Jet Propulsion Laboratory, California Institute of Technology under a contract with NASA.

Facilities: JWST (NIRCam, NIRSpec), MAST, IRSA, WISE, NEOWISE, Spitzer, ALMA

APPENDIX

A. POSITION AND PROPER MOTION OF THE PROTOSTAR FROM ALMA DATA

We took the proper motion of the B335 protostar into account, since any shock features of the outflow should be measured relative to the protostar, that is not directly detected at NIRCam wavelengths. Since B335 is a well-studied object, numerous observations are available publicly. We have selected the highest spatial resolution continuum data publicly available in mid 2024 from the ALMA Science Archive. The data used here are from [Maury et al. \(2018\)](#) [Bjerkeli et al. \(2019\)](#), [Imai et al. \(2019\)](#), [Okoda et al. \(2022\)](#) and other unpublished ALMA data included in the following list:

```

uid://A001/X11f/X7b PI name: Yen, Hsi-Wei 2014-09-02
uid://A001/X145/X2b3 PI name: Ruiz, Maria Teresa 2015-08-27
uid://A001/X2fe/X21 PI name: Evans, Neal 2016-07-17
uid://A001/X2c9/X17 PI name: Yen, Hsi-Wei 2016-07-24
uid://A001/X1284/X2059 PI name: Bjerkeli, Per 2017-10-08
uid://A001/X133d/X2eed PI name: Imai, Muneki 2019-06-23
uid://A001/X1590/X1e95 PI name: Jorgensen, Jes 2022-08-20
uid://A001/X1590/X1e91 PI name: Jorgensen, Jes 2022-08-20
uid://A001/X2d20/X2f92 PI name: Jorgensen, Jes 2023-04-12
uid://A001/X2df7/X600 PI name: Plunkett, Adele 2023-04-20
uid://A001/X2df7/X736 PI name: Yang, Yao-Lun 2023-04-21
uid://A001/X2d20/X1c3b PI name: Baek, Giseon 2023-05-25

```

These data were taken at a variety of frequencies, and with different configurations of ALMA, and therefore have a variety of angular resolutions. Since, to the best of current knowledge, the B335 protostar is an isolated single object at sub-mm and mm wavelengths, we use all these measurements to determine the proper motion of the protostar.

Different centroiding methods implemented in various python routines tend to give slightly different results. This has been studied and documented for the case of NIRISS data by [Goudfrooij \(2022\)](#). We use both the momentum based classical centroid algorithm as implemented in `photutils.aperture.ApertureStats` and the 2D-Gaussian fitting as implemented in `centroid_sources` with `centroid_func = centroid_2dg`.

We have included one older position measurement of the B335 protostar from [Reipurth et al. \(2002\)](#) from VLA configuration A observations at 3.6 cm wavelength, 8h of exposure time estimated position error $0''.05$, beam for B335 was $0''.32 \times 0''.28$. The source in B335 was identified as extended, interpreted as evidence for a compact thermal radio jet. The 2001 VLA position fits very well with the later, shorter wavelength ALMA observations, despite the wavelength difference and probably the difference in the excitation mechanism of the emission.

All ALMA positions and the VLA positions were reduced to barycentric coordinates using the distance of 165 pc. The parallax is small at ≈ 7 mas, but is of similar magnitude as the annual proper motion. From the fits of the VLA and ALMA positions of the B335 protostar shown in Figure 25, we get the ICRS position in degrees (J2000.0):

$$\alpha(t) = 294.25369864 + 2.62 \times 10^{-6} \times (t - 2000.0),$$

$$\delta(t) = 7.56940726 - 5.33 \times 10^{-6} \times (t - 2000.0) \text{ with } t \text{ in years.}$$

RA PM on sky [mas/yr] = 9.34, DEC PM in [mas/yr] = -19.17

The measured projected velocity of the B335 protostar is 16.7 km s^{-1} at a position angle of 154° .

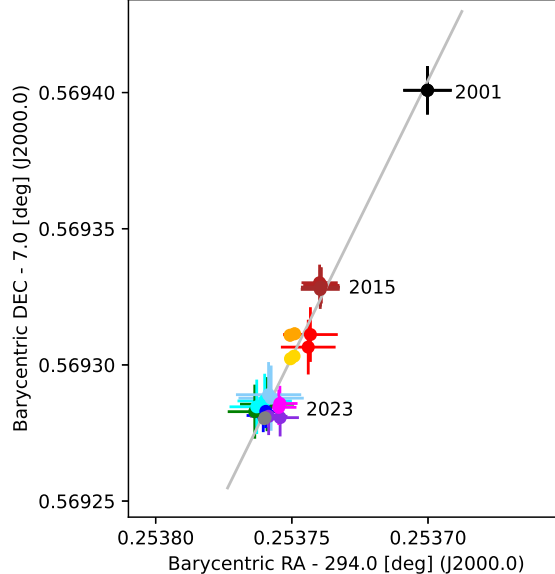


Figure 25. Proper motion of the B335 protostar from public ALMA data and one published VLA data point.

B. H₂O ICE COLUMN DENSITY FROM BACKGROUND STAR PHOTOMETRY

We obtained aperture photometry of most stars in our imaging field around B335. We compiled a list of star coordinates initially created by `daofind`. The list was manually curated to eliminate spurious detections in shock fronts or diffraction spikes, to eliminate close pairs of stars, and most extragalactic objects that could be visually identified as such.

In the shortest wavelength filters (F070W and F090W), our field in B335 appears blank. Therefore, every star in the field has at least one filter where it is not saturated and a precise position could be measured. The optical depth of the broad absorption feature of H₂O ice can be approximately measured using filter photometry. The ideal filters for this purpose would have been the NIRCam filters F250M, F300M, and F360M. However, since our program was primarily focused on obtaining slitless grism spectroscopy, we only obtained direct images in the F300M filter for H₂O ice photometry, and in the F277W and F356W filters that were also used for the WFSS.

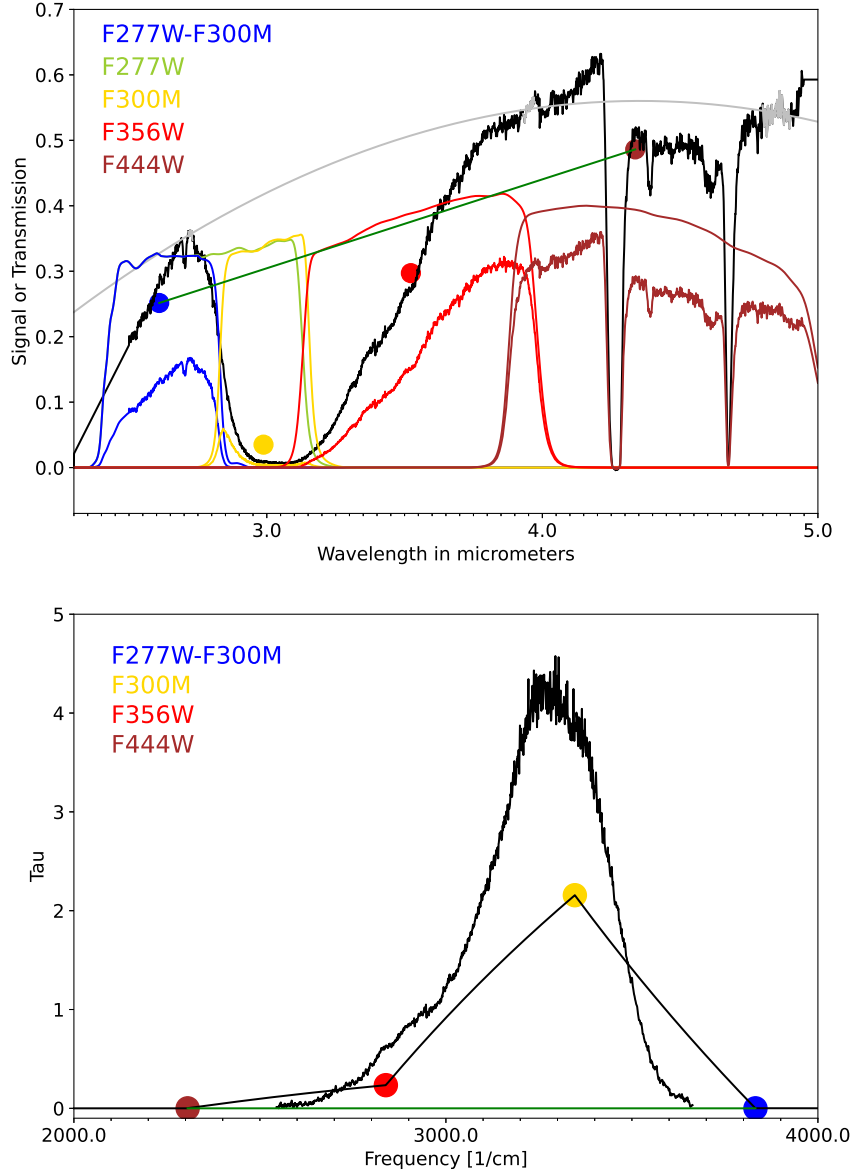


Figure 26. Top: spectrum of NIRS38 from McClure et al. (2023) shown as a black line. The continuum regions for the polynomial continuum fit are shown in grey. The transmission curves of the NIRCam filters are the smooth thin colored lines. The product of the spectrum and the transmission are shown in the same color as the filter transmission curves. Large filled circles indicate the effective wavelengths of the filters, and the spectrum signal integrated over the filter transmission. The green line is the linear interpolation of the continuum between the F277-F300M and F444W synthetic photometry points. Bottom: Optical depth τ vs. spacial frequency from the spectrum and from the linear interpolation of the synthetic photometry. Filled circles denote the individual filters, as in the top panel.

We performed aperture photometry with an aperture of 3 pixels radius in those filters on combined (...i2d) images to approximately measure the column density of H_2O ice in B335. The images were destriped by subtracting the median of the bottom 1/4 of data values, effectively a robust minimum, along each image row. Aperture photometry was done with an aperture of $0''.189$, using photutils. The sky brightness and some extended emission was locally subtracted using an annulus in the range of $0''.378 < r < 0''.629$.

The aperture correction was determined for each filter by doing the same aperture photometry, including sky annulus subtraction, on synthetic images of the psf, created by STPSF (formerly WebbPSF).

We used the following method to approximately measure the H_2O ice column density from the available photometry, illustrated in Figure 26. We show a high signal-to-noise spectrum of a heavily obscured background star behind the Chameleon I molecular cloud from McClure et al. (2023). In Figure 26, we also show the transmission curves of all the NIRCam filters used for that photometric column density measurement: F227W, F300M, F356W, and F444W. The F277W filter covers continuum in the lower part of its transmission range, but its upper half covers the H_2O ice absorption band. The F300M filter is narrower than the F277W filter, and covers the center of the H_2O ice band. As Figure 26 (top panel) shows, a synthetic photometric value using the difference of the transmission curves of F277W (green transmission curve) minus F300M (yellow transmission curve) gives a better approximation of the continuum shortward of the H_2O ice feature, and is shown as the blue transmission curve with an effective wavelength of $2.61\ \mu\text{m}$. The F300M filter (yellow) covers the center of the H_2O ice feature, and the F356W filter (red transmission curve) covers its long-wavelength wing. The F444W filter (brown transmission curve) covers spectral regions outside of the H_2O ice feature, but is affected by the narrow, though deep, absorption bands of CO_2 and CO. This filter therefore underestimates the flux in the continuum.

As an approximation, we use the synthetic “F277-F300M” flux and the F444W flux as continuum points, we linearly interpolate between those two points as an estimate of the continuum, and compute the optical depth τ as the \log_{10} of the flux ratio of the interpolated continuum and the measured flux at the effective wavelengths of the F300M and F356W filters. The resulting values of τ are shown in the bottom part of Figure 26. We then integrate this linearly interpolated τ spectrum over frequency in units of cm^{-1} .

For comparison and calibration, we also determine τ from the example spectrum, using a second order polynomial fit to the three continuum regions free of ice features and indicated in grey color in Figure 26 (top). The τ measured from the spectrum is the blue spectrum in Figure 26 (bottom).

The ratio of the spectral to the photometric τ measurement in this one example is 1.44, and we use this as our best estimate for the calibration factor to go from the photometric τ to the true spectroscopic τ .

C. COMPONENT ANALYSIS OF ICE ABSORPTION FEATURES

Ice absorption and scattering bands are detected throughout the outflow cones of B335. We analyze the set of 11 sight-lines extracted within the rectangular apertures identified in 16. The $3.0\ \mu\text{m}$ band of H_2O ices is severely saturated in all sight-lines and therefore not shown in Figure 20. The strong C–O stretching modes of CO_2 and CO at 4.25 and $4.67\ \mu\text{m}$, respectively, are detected everywhere. The CO_2 band is always saturated, and the CO ice band is saturated or nearly saturated in its core. The weaker 4.38 , 4.60 , and $4.90\ \mu\text{m}$ features, attributed to $^{13}\text{CO}_2$, OCN^- , and OCS ices, are detected in all sight-lines, while the ^{13}CO ice band at $4.78\ \mu\text{m}$ is seen in a few. Finally, the C–H stretch mode at $3.53\ \mu\text{m}$ is visible in a number of sight-lines, while in others it is limited by the low S/N of the continuum at those wavelengths.

Forests of emission lines of the ro-vibrational P- and R-branch transitions of gas-phase CO are visible (Figure 18) in the sight-lines close to the protostar. For the purpose of the ice component analysis, these were removed from the flux spectra following the procedure described in Boogert et al. (2022). Line fluxes were measured with Gaussian fits to the most isolated, highest quality emission lines, from which rotation diagrams were constructed. Linear fits to the observed data points in the rotation diagrams were then used to determine the strengths of all transitions, which were subsequently subtracted from the observed flux spectra. This yields spectra in which the ice absorption features are much less contaminated by CO lines, but preserve the full spectral sampling of the data, allowing for more accurate band profile and column density measurements for the spectra at the cavity apertures 0, 1, 2, and 3. The remaining apertures perhaps show weak CO emission lines as well, but their effect on the ice bands is small. Finally, any hydrogen emission lines were masked if they overlap with the ice features.

In order to analyze the profiles of the ice features and derive column densities, we derive local baselines with low-order polynomials. As is clear in Figure 20 27, cavity sight-line 0 shows a smoothly rising continuum level, that is

well fitted with a second-order polynomial in the 3.8–5.3 μm wavelength range. Most other sight-lines show a jump in the continuum level across the 4.27 μm CO_2 ice band. This jump is up at longer wavelengths, which is reversed from that seen toward JWST/NIRCam and NIRSpec observations of the Chamaeleon background stars published in McClure et al. (2023) and Dartois et al. (2024). For these background stars the jump is attributed to scattering by large ($\sim 0.9 \mu\text{m}$) sized grains. The reversed jump seen in the B335 cavity is reproduced in some of the higher inclination circumstellar disk models presented in Dartois et al. (2022) (their Figures 10 and 11). Such a jump is also distinctly present in the *AKARI* spectrum of the edge-on disk surrounding the low-mass YSO IRAS 04301+2247 (Aikawa et al. 2012, their Figure 3). This disk, like that of B335, is nearly completely edge-on. It is remarkable that the strength of the scattering jump relative to the observed continuum increases for sight-lines further away from the protostar. We speculate that this is due to a larger column of grains in the foreground for sight-lines closer to the star, less affected by scattering in the disk geometry. For the purpose of the ice analysis, we chose to fit a second-order polynomial to all sight-lines, excluding the long-wavelength side of the CO_2 band from the fits (Figure 27). This preserves scattering effects on the ice bands in the optical depth spectra.

In order to put the B335 ice bands in context, we fit the OCN^- , CO, and OCS ice bands with functions that were used in previous work, following the approach of Boogert et al. (2022). The OCN^- band was found to consist of two components, centered on 2165.7 and 2175.4 cm^{-1} (4.6174 and 4.5969 μm ; van Broekhuizen et al. 2005). The 2165.7 cm^{-1} component is consistent with solid OCN^- in polar environments, while the other component relates perhaps to CO bonding to the grain surfaces or to OCN^- in apolar environments (Öberg et al. 2011). We adopt the same decomposition procedure, by fitting two Gaussians, one at 2165.7 cm^{-1} (FWHM = 26 cm^{-1}) and one at 2175.4 cm^{-1} (FWHM = 15 cm^{-1}). The fitting was done simultaneously with those of the CO ice feature, since they overlap. The CO ice feature was found to consist of three components (Pontoppidan et al. 2003). The narrow, central component of CO in an apolar environment ($\text{CO}_{\text{apolar}}$) was fitted using a Gaussian function (peak wavelength 4.6731 μm , FWHM = 0.0076 μm). The broader component of CO in polar environments (CO_{polar}) was fitted with a Lorentzian (4.6806 μm , FWHM = 0.0232 μm), and a narrow short-wavelength component, perhaps due to CO in a CO_2 environment (CO_{blue}), was fitted with a Gaussian (4.6648 μm , FWHM = 0.0065 μm). Thus, the only variables in these fits are the peak optical depths. The OCS feature at $\sim 4.90 \mu\text{m}$, however, was fitted with an unconstrained Gaussian function. Examples of these fits are shown in Figure 28.

Due to the peak optical depths of > 4 , fits to this CO ice band—in particular that of the $\text{CO}_{\text{apolar}}$ component—are compromised by saturation effects. In addition, the presence of a hydrogen emission line near 4.7 μm limits the use of the long-wavelength wing to determine the strength of the CO_{polar} component. We find that, when fitting the extended wing, visible up to $\sim 4.75 \mu\text{m}$, with the CO_{polar} Lorentzian component, a significant fraction of the OCN^- band is consumed. Considering the overlap with gas-phase lines and possible scattering effects, we have limited the depth of the fitted CO_{polar} component to minimize the effects on the OCN^- band. Other than this, reasonable fits are obtained for the OCN^- band, showing a dominance of the long-wavelength component attributed to OCN^- in polar ice environments, in agreement with previous work on low- and high-mass YSOs (e.g., van Broekhuizen et al. 2005; Öberg et al. 2011; Boogert et al. 2022).

The OCS band has a Gaussian peak position and FWHM of $4.900 \pm 0.008 \mu\text{m}$ and $0.04 \pm 0.01 \mu\text{m}$, respectively, for all extracted positions across the B335 outflow cavities. This is comparable to the bulk of the massive YSO targets studied in Boogert et al. (2022, their Figure 13), and consistent with OCS embedded in CH_3OH -rich ices, and proton-irradiated H_2S - or SO_2 -containing ices. On the other hand, while the OCN^- /OCS column density ratio is constant across the outflow cavities, with a mean of 4.0 and a standard deviation of 0.4 (see also Figure 21), this is $\approx 50\%$ lower compared to massive YSOs Boogert et al. (2022, their Figure 13). An astrochemical discussion on the origin of this difference is beyond the scope of this paper.

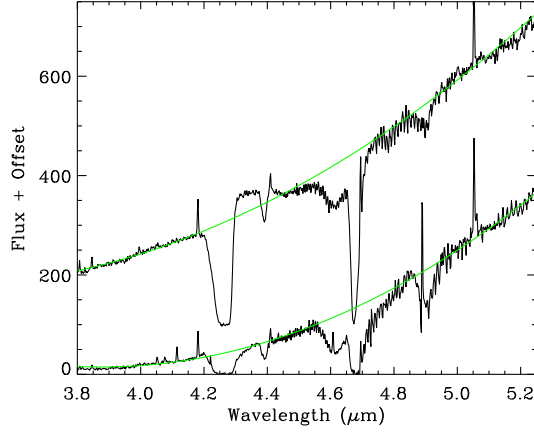


Figure 27. Polynomial baseline (green) used to derive the optical depth spectra for the ice features. The spectrum for position 8 in the B335 cavity is shown in the top figure, offset for clarity, and position 0 is shown at the bottom. Position 8, like most positions at larger distances from the central star, shows a distinct jump across the $4.25\text{ }\mu\text{m}$ CO_2 ice feature. We have assumed that this is caused by scattering on the ice feature and have excluded it from the baseline fits. Note that position 0 does not show this jump, while it increases for sight-lines further away from the protostar.

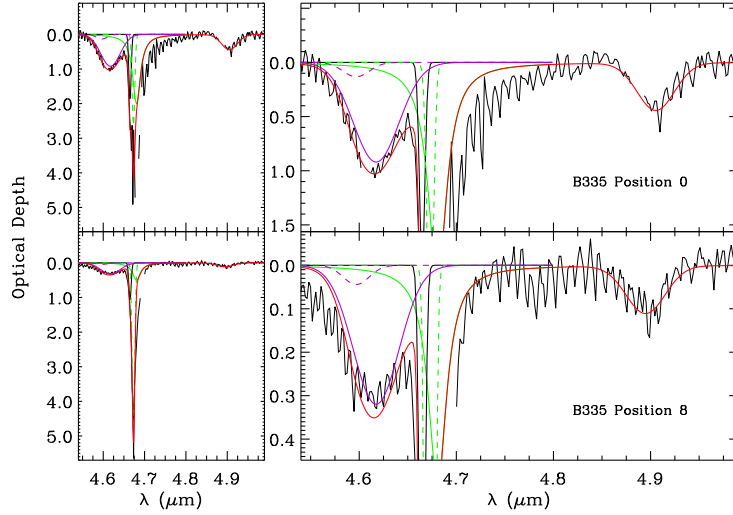


Figure 28. Optical depth spectra of two sight-lines (top and bottom) within the B335 outflow cavity: full scales in the left panels, and vertical zoom-ins on the right. Gaussian and Lorentzian fits to the CO ice bands (green: CO_{blue} , green dashed: $\text{CO}_{\text{apolar}}$, black: CO_{polar}) are shown, and Gaussian fits to the 2165.7 and 2175.4 cm^{-1} components of the OCN^- band (solid purple and dashed purple, respectively). The OCS band at $4.90\text{ }\mu\text{m}$ is fitted with a single Gaussian. The red line is the sum of all components.

REFERENCES

Aikawa, Y., Kamuro, D., Sakon, I., et al. 2012, *A&A*, 538, A57. doi:10.1051/0004-6361/201015999

Aspin, C., Reipurth, B., Beck, T. L., et al. 2009, *ApJL*, 692, 2, L67. doi:10.1088/0004-637X/692/2/L67

Avila, R., Rodríguez, L. F., & Curiel, S. 2001, *RMxAA*, 37, 201

Barnard, E. E., Frost, E. B., & Calvert, M. R. 1927, [Washington] Carnegie institution of Washington, 1927.

Bertrang, G., Wolf, S., & Das, H. S. 2014, *A&A*, 565, A94. doi:10.1051/0004-6361/201323091

Bjerkeli, P., Ramsey, J. P., Harsono, D., et al. 2019, *A&A*, 631, A64. doi:10.1051/0004-6361/201935948

Bjerkeli, P., Ramsey, J. P., Harsono, D., et al. 2023, *A&A*, 677, A62. doi:10.1051/0004-6361/202245195

Boogert, A. C. A., Brewer, K., Brittain, A., et al. 2022, *ApJ*, 941, 1, 32. doi:10.3847/1538-4357/ac9b4a

Bouilloud, M., Fray, N., Bénilan, Y., et al. 2015, *MNRAS*, 451, 2145. doi:10.1093/mnras/stv1021

Brunken, N. G. C., Rocha, W. R. M., van Dishoeck, E. F., et al. 2024, *A&A*, 685, A27. doi:10.1051/0004-6361/202348718

Cabedo, V., Maury, A., Girart, J. M., et al. 2021, *A&A*, 653, A166. doi:10.1051/0004-6361/202140754

Chu, L. E. U. & Hodapp, K. W. 2021, *ApJ*, 918, 2. doi:10.3847/1538-4357/ac0ae8

Connelley, M. S., Hodapp, K. W., & Fuller, G. A. 2009, *AJ*, 137, 3494. doi:10.1088/0004-6256/137/3/3494

Contreras Peña, C., Lee, J.-E., Herczeg, G., et al. 2025, Journal of Korean Astronomical Society, 58, 209. doi:10.5303/JKAS.2025.58.2.209

Dartois, E., Noble, J. A., Ysard, N., et al. 2022, *A&A*, 666, A153. doi:10.1051/0004-6361/202243929

Dartois, E., Noble, J. A., Caselli, P., et al. 2024, *Nature Astronomy*, 8, 359. doi:10.1038/s41550-023-02155-x

Dawes, A., Mason, N. J., & Fraser, H. J. 2016, *Physical Chemistry Chemical Physics (Incorporating Faraday Transactions)*, 18, 2, 1245. doi:10.1039/C5CP05299H

Evans, N. J., Yang, Y.-L., Green, J. D., et al. 2023, *ApJ*, 943, 90. doi:10.3847/1538-4357/aca38

Federman, S. A., Megeath, S. T., Rubinstein, A. E., et al. 2024, *ApJ*, 966, 41. doi:10.3847/1538-4357/ad2fa0

Federman, S. A., Megeath, S. T., Caratti o Garatti, A., Narang, M., Tyagi, H., Evans, N. J. II, Kimmig, C. N., Tychoniec, L., Beuther, H., Stutz, A., Manoj, P., Gutermuth, R., Bourke, T. L., Green, J., Hartmann, L., Klaassen, P., Kuiper, R., Looney, L. W., Nazari, P., Stanke, T., Watson, D. M., Yang, Y.-L., & Zakri, W. 2026, arXiv:2601.09587

Frerking, M. A. & Langer, W. D. 1982, *ApJ*, 256, 523. doi:10.1086/159928

Frerking, M. A., Langer, W. D., & Wilson, R. W. 1987, *ApJ*, 313, 320. doi:10.1086/164970

Gálffy, M. & Olofsson, G. 2007, *A&A*, 475, 281. doi:10.1051/0004-6361:20077889

Gardner, J. P., Mather, J. C., Abbott, R., et al. 2023, *PASP*, 135, 068001. doi:10.1088/1538-3873/acd1b5

Gerakines, P. A., Materese, C. K., & Hudson, R. L. 2025, *MNRAS*, 537, 3, 2918. doi:10.1093/mnras/staf192

Goudfrooij, P. 2022, Doc: JWST-STScI-008116, SM-12, (Feb. 9, 2022)

Goldsmith, P. F., Snell, R. L., Hemeon-Heyer, M., et al. 1984, *ApJ*, 286, 599. doi:10.1086/162635

González-Alfonso, E., Wright, C. M., Cernicharo, J., et al. 2002, *A&A*, 386, 1074. doi:10.1051/0004-6361:20020362

Goorvitch, D. 1994, *ApJS*, 95, 535. doi:10.1086/192110

Green, J. D., Evans, N. J., Jørgensen, J. K., et al. 2013, *ApJ*, 770, 2, 123. doi:10.1088/0004-637X/770/2/123

Hirano, N., Kameya, O., Nakayama, M., et al. 1988, *ApJL*, 327, L69. doi:10.1086/185142

Hodapp, K.-W. 1984, *A&A*, 141, 255.

Hodapp, K.-W. 1987, *ApJ*, 319, 842. doi:10.1086/165502

Hodapp, K.-W., Hora, J. L., Rayner, J. T., et al. 1996, *ApJ*, 468, 861. doi:10.1086/177742

Hodapp, K.-W. 1998, *ApJL*, 500, L183. doi:10.1086/311412

Hodapp, K. W. & Bressert, E. 2009, *AJ*, 137, 3501. doi:10.1088/0004-6256/137/3/3501

Hodapp, K. W., Chini, R., Watermann, R., et al. 2012, *ApJ*, 744, 1, 56. doi:10.1088/0004-637X/744/1/56

Hodapp, K. W., Chu, L. L., Greene, T., et al. 2024, *AJ*, 167, 102. doi:10.3847/1538-3881/ad1b55

Hollenbach, D. & McKee, C. F. 1979, *ApJS*, 41, 555. doi:10.1086/190631

Hollenbach, D. & McKee, C. F. 1980, *ApJL*, 241, L47. doi:10.1086/183358

Hollenbach, D. & McKee, C. F. 1989, *ApJ*, 342, 306. doi:10.1086/167595

Hubble, E. P. 1916, *ApJ*, 44, 190. doi:10.1086/142284

Imai, M., Oya, Y., Sakai, N., et al. 2019, *ApJL*, 873, L21. doi:10.3847/2041-8213/ab0c20

Kandori, R., Saito, M., Tamura, M., et al. 2020, *ApJ*, 891, 55. doi:10.3847/1538-4357/ab6f07

Keene, J., Davidson, J. A., Harper, D. A., et al. 1983, *ApJL*, 274, L43. doi:10.1086/184147

Kim, C.-H., Lee, J.-E., Peña, C. C., et al. 2024, *ApJ*, 961, 1, 108. doi:10.3847/1538-4357/ad1400

Lada, C. J., Lada, E. A., Clemens, D. P., et al. 1994, *ApJ*, 429, 694. doi:10.1086/174354

Lightfoot, J. & Scholz, A. 2025, *MNRAS*, 540, 1, 52. doi:10.1093/mnras/staf708

Lightfoot, J. F. 1989, *MNRAS*, 239, 665. doi:10.1093/mnras/239.2.665

Le Gouellec, V. J. M., Maury, A. J., & Hull, C. L. H. 2023, *A&A*, 671, A167. doi:10.1051/0004-6361/202244865

Maury, A. J., Girart, J. M., Zhang, Q., et al. 2018, *MNRAS*, 477, 2760. doi:10.1093/mnras/sty574

McClure, M. K., Rocha, W. R. M., Pontoppidan, K. M., et al. 2023, *Nature Astronomy*, 7, 431. doi:10.1038/s41550-022-01875-w

Mestel, L., & Spitzer, L. 1956, *MNRAS*, 116, 503

Okuda, Y., Oya, Y., Imai, M., et al. 2022, *ApJ*, 935, 136. doi:10.3847/1538-4357/ac7ff4

Öberg, K. I., Boogert, A. C. A., Pontoppidan, K. M., et al. 2011, *ApJ*, 740, 2, 109. doi:10.1088/0004-637X/740/2/109

Olofsson, S. & Olofsson, G. 2009, *A&A*, 498, 455. doi:10.1051/0004-6361/200811574

Pontoppidan, K. M., Schöier, F. L., van Dishoeck, E. F., et al. 2002, *A&A*, 393, 585. doi:10.1051/0004-6361:20021056

Pontoppidan, K. M., Fraser, H. J., Dartois, E., et al. 2003, *A&A*, 408, 981. doi:10.1051/0004-6361:20031030

Ray, T. P. & Ferreira, J. 2021, *NewAR*, 93, 101615. doi:10.1016/j.newar.2021.101615

Reipurth, B., Heathcote, S., & Vrba, F. 1992, *A&A*, 256, 225

Reipurth, B., Rodríguez, L. F., Anglada, G., et al. 2002, *AJ*, 124, 1045. doi:10.1086/341172

Reipurth, B. 2008, in *Handbook of Star Forming Regions, Volume II*, ed. B. Reipurth (San Francisco, CA: ASP), 847

Rieke, M. J., Kelly, D. M., Misselt, K., et al. 2023, *PASP*, 135, 028001. doi:10.1088/1538-3873/acac53

Rocha, W. R. M., Perotti, G., Kristensen, L. E., et al. 2021, *A&A*, 654, A158. doi:10.1051/0004-6361/202039360

Rubinstein, A. E., Evans, N. J., Tyagi, H., et al. 2024, *ApJ*, 974, 112. doi:10.3847/1538-4357/ad6b92

Safron, E. J., Fischer, W. J., Megeath, S. T., et al. 2015, *ApJL*, 800, 1, L5. doi:10.1088/2041-8205/800/1/L5

Shu, F. H., Adams, F. C., & Lizano, S. 1987, *ARA&A*, 25, 23. doi:10.1146/annurev.aa.25.090187.000323

Slavíckinska, K., van Dishoeck, E. F., Tychoniec, L., et al. 2024, *A&A*, 688, A29. doi:10.1051/0004-6361/202449785

Slavičinská, K., Coone, C., Benz, B., Linnartz, H., Boogert, A. C. A., & Chuang, K.-J. 2025, *ACS Earth Space Chem.*, 9, 2148, doi:10.1021/acsearthspacechem.5c00134

Stutz, A. M., Rubin, M., Werner, M. W., et al. 2008, *ApJ*, 687, 389. doi:10.1086/591789

van Broekhuizen, F. A., Pontoppidan, K. M., Fraser, H. J., et al. 2005, *A&A*, 441, 1, 249. doi:10.1051/0004-6361:20041711

Vrba, F. J., Luginbuhl, C. B., Strom, S. E., et al. 1986, *AJ*, 92, 633. doi:10.1086/114194

Wang, S. & Chen, X. 2019, *ApJ*, 877, 116

Wang, W. et al. 2025, arXiv:2502.20442

Watson, D. M. 2020, *Research Notes of the American Astronomical Society*, 4, 88. doi:10.3847/2515-5172/ab9df4

Wright, E. L., Eisenhardt, P. R. M., Mainzer, A. K. et al., *AJ*, 140, 1868

Yen, H.-W., Takakuwa, S., Ohashi, N., & Ho, P. T. P. 2015, *ApJ*, 799, 193